SYNAPTIC RELEASE POTENTIATION AT AGING AUDITORY RIBBON SYNAPSES

Running title: Synaptopathy at aging auditory ribbon synapses

Thibault PEINEAU[1,2#], Séverin BELLEUDY[1#], Susanna PIETROPAOLO[3], Yohan BOULEAU[1,2] and Didier DULON[1,2*]

[1]Neurophysiologie de la Synapse Auditive, INSERM UMRS 1120, Bordeaux Neurocampus, Université de Bordeaux, 33076 Bordeaux, France

[2] Institut de l'Audition, Centre Institut Pasteur/Inserm, 63 rue de Charenton, 75012 Paris

[3] INCIA, UMR 5287, CNRS, University of Bordeaux, Bat B2, Allée Geoffroy St. Hilaire, CS 50023, 33615, Pessac Cedex, France.

[*] Corresponding author: Didier DULON
didier.dulon@inserm.fr

# First co-authors, contributed equally to the study

Keywords: Auditory hair cells, Synaptic ribbons, Synaptopathy, Hyperacusis, Ca^{2+} channels, Exocytosis

Conflict of Interest
The authors declare that the research was conducted in the absence of any commercial or financial relationships that could be construed as a potential conflict of interest.

Author Contributions
DD designed research; SB, TP, YB and DD performed research and analyzed the data. SP performed the Acoustic Startle Experiments. DD wrote the paper.

Funding & acknowledgments
This work was supported by a grant from the Fondation Pour l'Audition to DD (IDA CLINICAL TRANSLA - 010703E), and from the French Society of Audioprosthesis professionals, Entendre SAS (Saint Cyr l'Ecole 78210 France). Part of the content of the manuscript has previously appeared as a preprint online at bioRxiv https://doi.org/10.1101/2020.05.15.097550

ABSTRACT

Age-related hidden hearing loss is often described as a cochlear synaptopathy that results from a progressive degeneration of the inner hair cell (IHC) ribbon synapses. The functional changes occurring at these synapses during aging are not fully understood. Here, we characterized this aging process in IHCs of C57BL/6J mice, a strain which is known to carry a cadherin23 mutation and experiences early hearing loss with age. These mice, while displaying a large increase in auditory brainstem thresholds due to 50 % loss of IHC synaptic ribbons at middle age (postnatal day 365), paradoxically showed enhanced acoustic startle reflex suggesting a hyperacusis-like response. The auditory defect was associated with a large shrinkage of the IHCs' cell body and a drastic enlargement of their remaining presynaptic ribbons which were facing enlarged postsynaptic AMPAR clusters. Presynaptic Ca^{2+} microdomains and the capacity of IHCs to sustain high rates of exocytosis were largely increased, while on the contrary the expression of the fast repolarizing BK channels, known to negatively control transmitter release, was decreased. This age-related synaptic plasticity in IHCs suggested a functional potentiation of synaptic transmission at the surviving synapses, a process that could partially compensate the decrease in synapse number and underlie hyperacusis.

INTRODUCTION

Age-related hearing loss (ARHL or presbycusis) is the most prevalent form of sensory disability in human populations and adversely affects the quality of life of many elderly individuals. Simultaneously with ARHL, chronic tinnitus and hyperacusis often develop due to abnormal neural activity in the central auditory system whose origin may arise from cochlear pathologies (for review see Knipper et al., 2013). The development of ARHL has been generally considered to be associated with primary degeneration of cochlear hair cells, with secondary deafferentation associating degeneration of spiral ganglion neurons and ribbon synapses. However, recent studies have resulted in a paradigm shift in the understanding of the early cause of ARHL (Kujawa and Liberman, 2015; 2019). During aging, hearing thresholds in the elderly often remain normal but speech intelligibility become hampered, especially in noisy environment. This pathology in the elderly is referred as hidden hearing loss and has been proposed to be caused in mice by an early loss of ribbon synapses contacting the inner hair cells (IHCs), well before any major loss of hair cells and spiral ganglion neurons (Stamataki et al., 2006). While glutamate excitotoxicity, resulting in nerve terminal swelling, has been proposed to play a role in the setting of noise-induced hearing loss (Pujol and Puel, 1999; Hu et al., 2020), the molecular mechanisms underlying the degeneration of the cochlear ribbon synapses during aging remain to be elucidated. Oxidative damage due to an increase in ROS levels seems to plays a crucial role in ARHL (Fu et al., 2018) but how the ribbon synapses are functionally affected remain unknown.

The C57BL/6J inbred strain of mice has been extensively used as model for ARHL (Johnson et al., 1997; Spongr et al., 1997; Hequembourg and Liberman, 2001; Bartolomé et al., 2002; Henry, 2002). This mouse strain carries a cadherin23 mutation (*Cdh23* ^{753A}, also known as *Ahl*), which affects inner ear structures, characterized by progressive degeneration of ribbon synapses and spiral ganglion neurons, and results in age-related hearing loss. *Ahl* is a recessive single nucleotide mutation at 753 (G=>A) on the *Cdh23* gene on mouse chromosome 10 (Noben-Trauth et al., 2003). *Cdh23* encodes cadherin 23, a protein necessary for inner ear development and maintenance of the sensory hair cell structures, in particular the tip and lateral links of the stereocilia at the hair bundle (Siemens et al., 2004; Söllner et al., 2004; Kazmierczak et al., 2007; Michel et al., 2005; Lagziel et al., 2005), but growing anatomical evidence also suggests that synaptic rearrangements on sensory hair cells also contribute to auditory functional decline in C57BL/6J mice (Stamataki et al., 2006; Zachary and Fuchs, 2015; Jiang et al., 2015; Jeng et al., 2021). Surprisingly, aging C57BL/6J mice,

102 although showing cochlear ribbon synapse degeneration and hearing loss, display increased
103 acoustic startle reflex amplitudes (Ouagazzal et al., 2006; Ison and Allen, 2003; Ison et al.,
104 2007) and a time increase in recovery from ABR short-term adaptation (Walton et al., 1995).
105 Whether this exaggerated startle reflex can be explained by functional changes of cochlear
106 hair cell ribbon synapses remain to be explored. Our present study will show that aged
107 C57BL/6J mice, while losing nearly up to 50 % of their IHC ribbon synapses, have IHCs with
108 reduced BK channel clusters, larger remaining presynaptic ribbons (with increased Ca^{2+}
109 microdomains and larger sustained exocytotic responses) facing postsynaptic afferent boutons
110 with larger AMPAR clusters. All these features indicated that synaptic release potentiation
111 occur at auditory IHC ribbon synapses during aging. This age-related synaptic plasticity could
112 be viewed as compensatory mechanisms of the decrease IHC synapse number and may
113 explain the hyperacusis-like startle reflex observed in aged C57BL/6J mice.
114

115 ## RESULTS

116 ### Increased ABR thresholds and hyperacusis-like effect on ASR

117 As previously described (Zheng et al., 1999; Zhou et al., 2006), CBA/J mice, used here as a
118 reference, showed no sign of rapid degradation of their hearing function with aging, as
119 attested by constant click ABR thresholds near 15 dB SPL up to one year of age (Fig.1A). On
120 the contrary, C57BL/6J mice, carrying the *Cdh23*^{753A} mutation, displayed an early progressive
121 increase in ABR thresholds with aging (Fig.1A). Hearing thresholds started to increase
122 significantly at postnatal day P180 to reach a mean 50 dB increase at P365 (click ABR
123 thresholds above 65 dB SPL) as compared to young mature P30 mice. Distortion product
124 otoacoustic emissions (DPOAEs) in P365 C57BL/6J mice were still present but significantly
125 reduced, indicating that the electromechanical activity of the outer hair cells (OHCs) was also
126 affected (Fig.1D). However, counting hair cells on surface preparations of organs of Corti
127 from these P365 mice, in the mid-cochlea region (8-16 kHz), indicated only a moderate loss
128 of OHCs and IHCs (statistically not significant; Fig.2E), in good agreement with the study of
129 Zachary and Fuchs (2015). This moderate loss of OHCs suggested that the profound hearing
130 loss occurring at P365 in C57BL/6J mice arose from additional factors than a simple
131 alteration of the cochlear amplifier. We then compared the amplitude on the ABR wave-I as a
132 function of sound intensity in young and old mice. The wave-I is known to result from the
133 synchronous activity of the auditory nerve fibers and can provide an objective measure of
134 ribbon synapses loss when measured at high sound intensity above 70 dB SPL. In P365 old

mice, ABR wave-I amplitudes were largely reduced as compared to young mature P30 mice, even at high sound intensity when IHCs are directly stimulated and bypass the amplification process of the OHCs (Fig.1B). The large decrease in wave-I amplitude indicated a decreased number of auditory nerve fibers activated by sound and/or a decrease in their firing rate or synchrony. The latencies of the ABR wave-I were also significantly increased suggesting again that the IHC ribbon synapses are affected (Fig.1C).

Surprisingly, at lower sound intensities tested (between 20-35 dB above background noise level), the strength of the acoustic startle reflex (ASR) was found larger in old P365 C57BL/6J mice as compared to young P60, indicating hyperacusis reactivity (Fig 1.E). The origin of this acoustic hypereactivity at low sound intensities could arise from central neural reorganization (Willott 1996) and be consecutive to functional defect of the IHC ribbon synapses in aging C57BL/6J mice that we are going to characterize in this study. At loud sound intensities, 45 dB above background noise, the amplitude of the ASR responses were however diminished in old mice, likely reflecting the increase in ABR thresholds due to a drastic decrease in the number of ribbon synapses per IHCs.

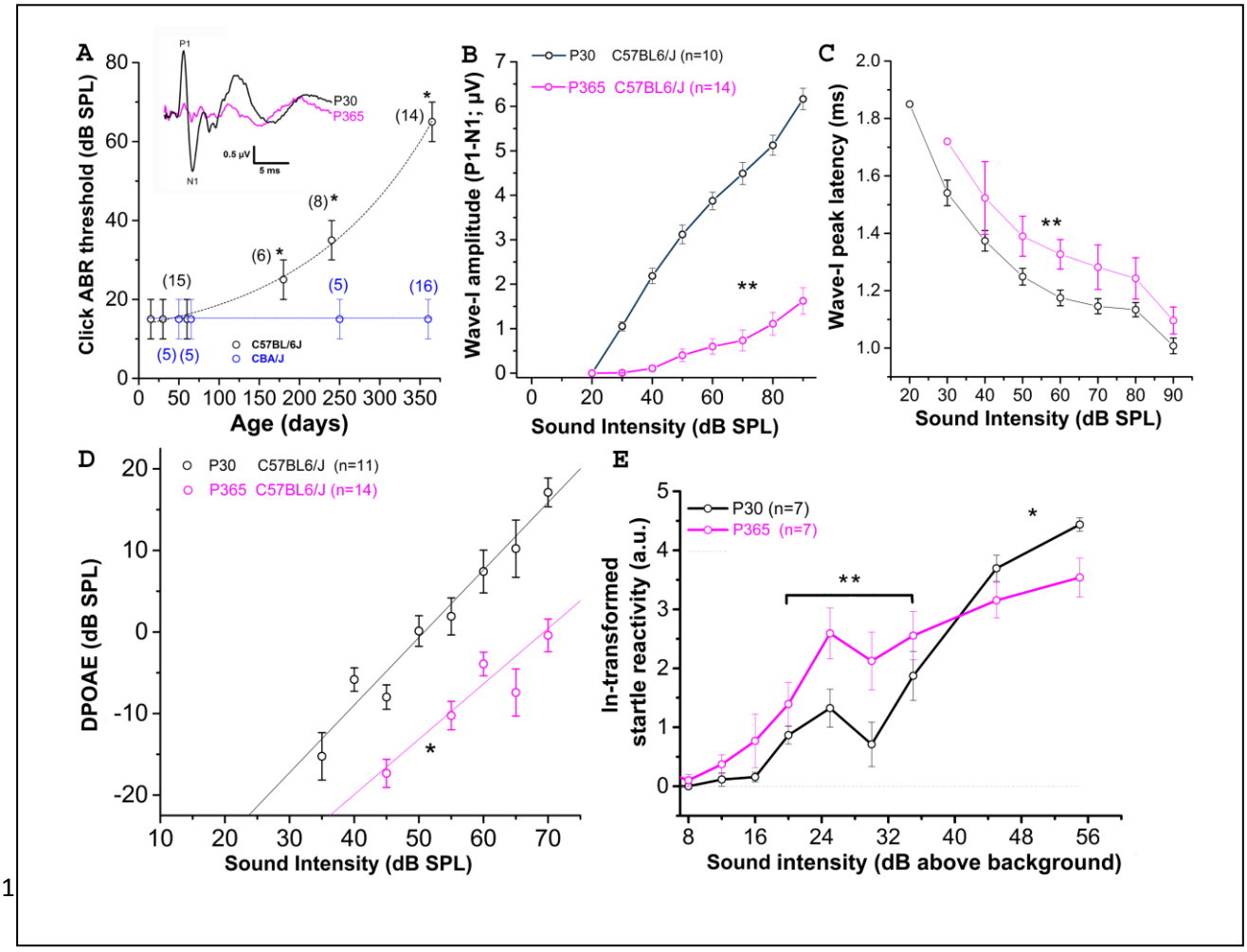

Figure 1. Sensorineural hearing loss with Aging in C57BL/6J mice. (**A**) Click-ABR thresholds as a function of age in CBA/J mice (blue; n = 5 to 16) and C57BL/6J mice (black, n = 6 to 15). For each strain, asterisks indicate significant difference with p<0.05 as compared to P30 mice (two-way ANOVA). Inset show comparative mean ABR waves at 70 dB SPL in P30 and P365 C57BL/6J mice. (**B**) Wave-I amplitude (P1-N1) as a function of sound intensity in young P30 (black) and old P365 (pink) C57BL/6J mice. Asterisks indicate significant difference with p<0.05 (two-way ANOVA; p = 0.001). (**C**) Latency to reach peak amplitude of wave-I as a function of sound intensity. Significantly different with p=0.003 between 80 to 50 dB SPL (two-way ANOVA; n is indicated in graph B). (**D**) Distortion products otoacoustic emissions (DPOAEs; 2f1-f2 with f1 = 12.73 kHz and f2 = 15,26 kHz) as a function of sound intensity in young P30 (black) and old P360 (pink) C57BL/6J mice. Asterisk indicated significant difference with p<0.05 (two-way ANOVA, p = 0.01). (**E**) Startle reactivity to acoustic stimulation. The intensity of startle reaction (in mV) was ln-transformed and obtained through two conditions of white-noise bursts of 20 and 40 ms. Note that below 35 dB above background the startle reaction is increased at P360 whereas at 45 and 55 dB above background the startle reaction is decreased compared to P30 mice. Asteriks indicated significant difference with p<0.05 (two-way ANOVA, p = 0.007 between 20-35 dB and p = 0.005 between 45-55 dB).

Drastic loss of IHC synaptic ribbons with aging

Confocal immunofluorescence imaging of the synaptic ribbons in IHCs from C57BL/6J mice, in the cochlear region encoding between 8-16 kHz, showed a progressive and large decrease in the number of synaptic ribbons with aging, from 16.3 ± 0.3 ribbons/IHC at P15 to 8.7 ± 0.5 ribbons/IHC at P365 (Fig.2A-C). This nearly 50% loss of synaptic ribbons in IHCs of C57BL/6J mice at P365 was in good agreement with previous studies (Zachary and Fuchs, 2015; Jeng et al., 2020). Counting the spiral ganglion neurons in the mid-frequency region of the cochlea (8-16 kHz) showed a mean 20 % loss of neuron in P365 mice as compared to P30 mice (Fig.2D-F). Remarkably, the age-related loss of neurons, averaging 20 %, was much less pronounced than the loss of IHC synaptic ribbons (50 %), suggesting that there was a large number of neurons surviving without dendritic/synaptic projection toward the organ of Corti as previously shown by Stamataki et al. (2006).

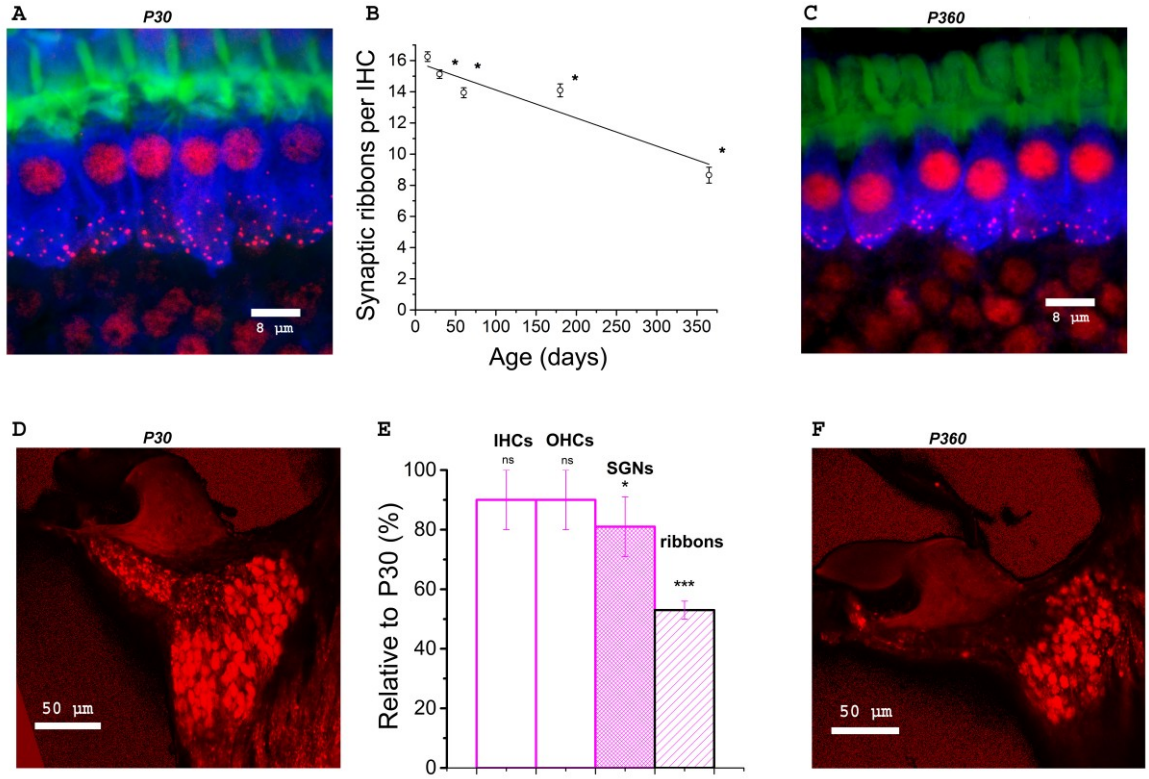

Figure 2. Synaptic ribbon loss in aging IHCs and comparative density of spiral ganglion neurons**. (A-C**) Confocal immunofluorescence imaging of IHCs from P30 and P360 C57BL/6J mice. Image resulted from stack reconstructions of 22 slices of 0.3 µm thickness, showing F-actin (green, labeling the hair bundles), otoferlin (blue; a synaptic Ca^{2+} sensor labeling the entire IHC body) and synaptic ribbons (Ribeye/CtBP2, red dots). The white bars indicated 8 µm. (**B**) Plot of synaptic ribbon counts per IHC as a function of age in C57BL/6J mice (black) in the mid-frequency cochlear region (8-16 kHz). Asterisks indicate significant difference with $p<0.05$ (comparison with P15 C57BL/6J mice, one-way ANOVA post-hoc Tukey test). 203, 306, 306, 306, 295 ribbons were respectively analyzed at P15, P30, P60, P180, P365 in 3 to 5 mice at each age. (**D-F**) Confocal immunofluorescence imaging of cochlear transversal sections from P30 and P360 mice (8-16 kHz area) where neurons and their afferent dendrites are labeled with dextran amines 3000. (**E**) Analyzed in the mid-cochlea (8-16kHz), comparative histogram of hair cells counts, SGNs and synaptic ribbons (3 mice at each age relative to young mature P30 C57BL/6J mice. The asterisks indicated statistical difference with $p < 0.05$ (from left to right $p = 0.37$, $p = 0.14$, $p = 0.020$ for SGNs and $p = 1.01E-14$ for ribbons, using unpaired t-test). Note the reduction in SGNs and the drastic decrease of the fluorescent labeling of the afferent nerve fibers projecting to the organ of Corti.

Enlarged presynaptic ribbons associated with larger postsynaptic AMPAR clusters

When analyzing the 3-D imaging reconstruction of the IHC synaptic ribbons from P365 C57BL/6J IHCs from high resolution confocal STED immunofluorescent sections, we found that these structures displayed a progressive increase in their mean size (volume) as compared to young P15 mice (Fig.3A). The mean volume of the synaptic ribbons increased nearly three-fold between P15 and P365 (Fig.3B). Interestingly, the increase in size of the ribbons started very early after P30, an age at which their number also started to decrease (Fig.2B) while hearing thresholds were still normal (Fig.1A).

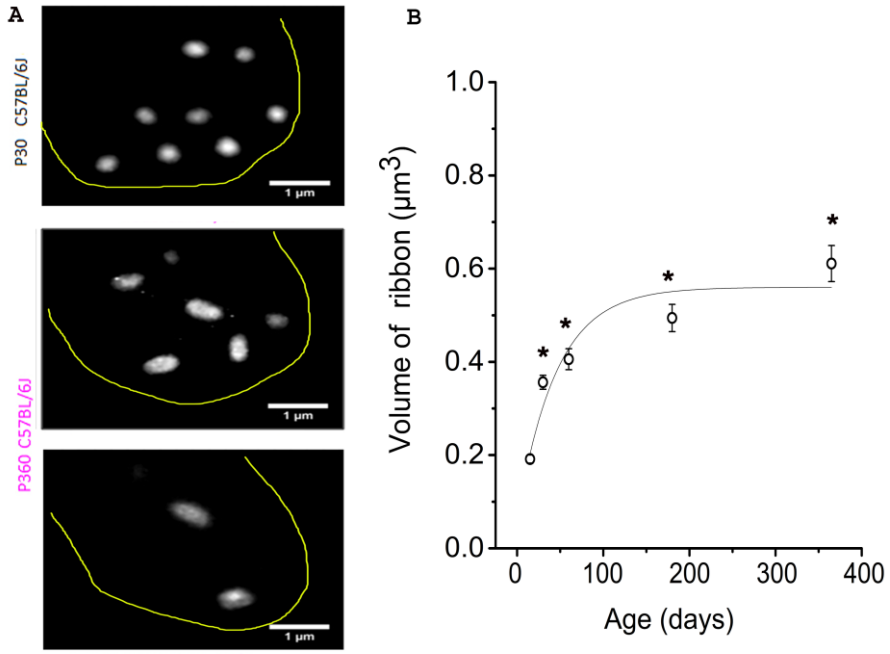

Figure 3. IHC synaptic ribbons progressively increased in size with aging. (**A**) Example of high magnification confocal STED images (stack reconstruction of five 0.25 µm slices). The yellow line delineates the IHC contour. Ribbons were less numerous and larger in size in IHCs from P365 C57BL/6J mice. (**B**) The mean volume of the IHC synaptic ribbons was calculated in the mid-cochlear region (encoding 8-16 kHz), using the plugin 3D-Object counter of ImageJ, and was plotted as a function of age: P15 (203 ribbons - 40 IHCs - 3 mice), P30 (306 ribbons - 98 IHCs - 5 mice), P60 (306 ribbons - 95 IHCs - 3 mice), P180 (306 ribbons - 67 IHCs - 3 mice), P365 (295 ribbons - 43 IHCs - 3 mice). As indicated by the asterisks, when comparing with P15, the mean volume of the ribbons started significantly to increase significantly from P30 ($p<0.05$; one-way ANOVA).

We next investigated the changes occurring with aging in the spatial distribution of the synaptic ribbons at the basolateral membrane of the IHCs. It is worth recalling that larger presynaptic ribbons associated to low-spontaneous-rate afferent fibers are usually found at the modiolar side of the IHCs (i.e. the baso-lateral curved side of the IHCs directed toward the spriral ganglion neuron) while smaller ribbons associated with high-spontaneous-rate afferent fibers predominates at the pillar side (Liberman, 1982; Liberman et al., 2011). We found that, while a larger proportion of synaptic ribbons distributed at the modiolar side in young P30 IHCs (~60 %), the surviving ribbons in old P365 IHCs were evenly distributed at the pillar and modiolar side (Fig.4A-B). The loss of synaptic ribbons with aging was more pronounced at the modiolar side, ie at the side where most of the low-spontaneous (high threshold) fibers make contact to IHCs (Fig 4C). An increase in volume was noted both in pillar and modiolar ribbons (Fig 4D). Unlike young P30 IHCs, old P365 IHCs had modiolar and pillar ribbons with similar volume (0.7 ± 0.1 μm^3 and 0.57 ± 0.07 μm^3, respectively; not significantly different, unpaired t-test $p = 0.28$, Fig.4D). Similar preferential loss of synaptic modiolar

ribbons associated with an increase in ribbon volume was also reported after noise-induced hearing loss (Liberman and Kujawa, 2017; Hickman et al., 2020).

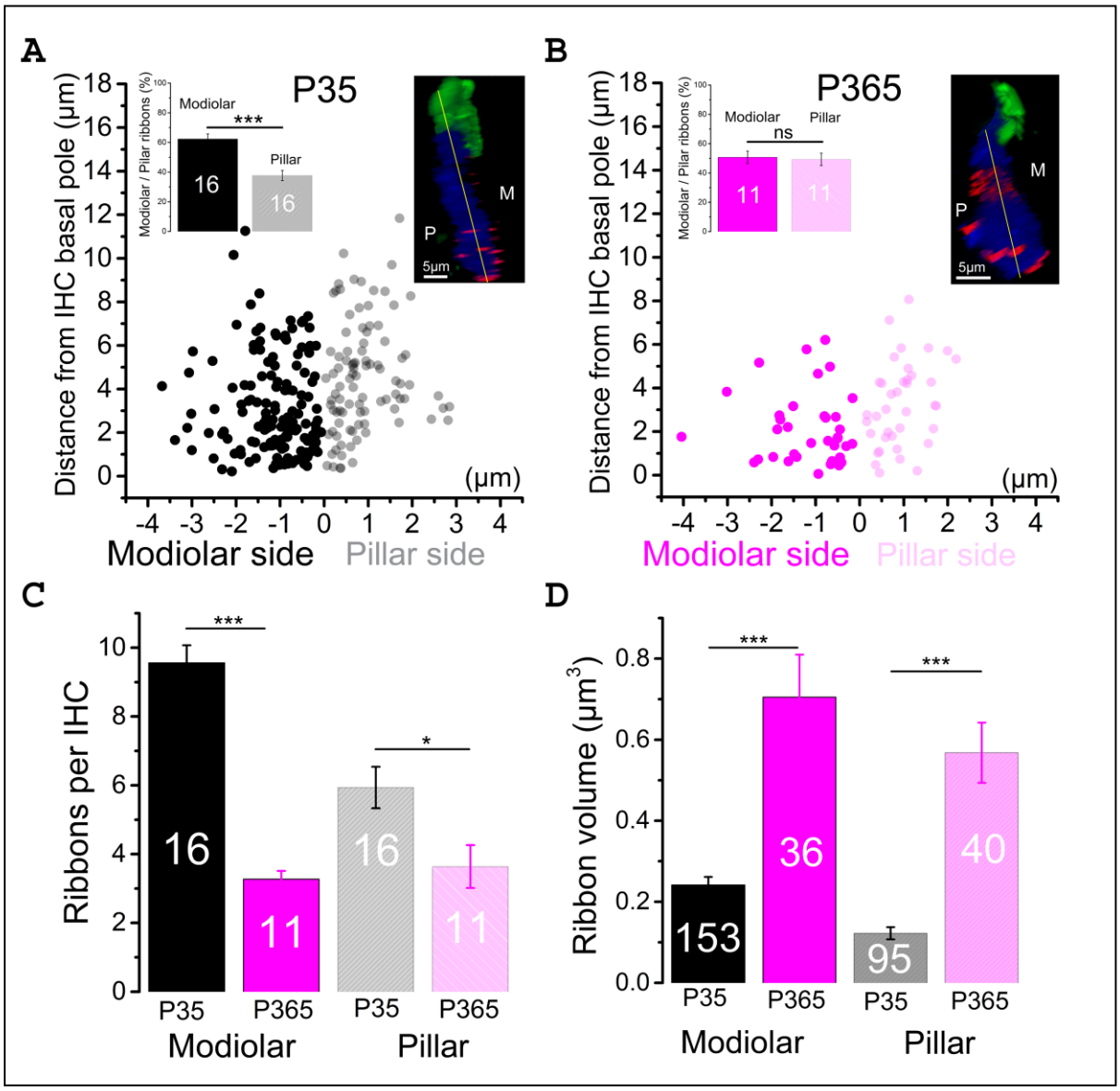

Figure 4. Modiolar vs pillar distribution of the synaptic ribbons with aging. (**A-B**) The distribution of IHC synaptic ribbons was splitted in two cell areas: P (pillar side) and M (Modiolar side). The two regions were determined using the K-means clustering method for each cell (see Methods). The yellow lines in the inset confocal images was drawn to arbitrarily delineate the frontier between pillar and modiolar ribbons (green labeling F-actin, blue Otoferlin and red the synaptic ribbons). Note that in young P30 IHCs (n=16), synaptic ribbons are preferentially localized in the modiolar region (62.3 ± 3.5 % vs 37.7 ± 3.5; unpaired t-test p = 2.07 E-5). In old P365 IHCs (n=11), the remaining ribbons equally distributed in the modiolar and pillar side (50.7 ± 4.0 % vs 49.3 ± 4.0 %, unpaired t-test; p = 0.81). (**C**) Synaptic ribbons were significantly loss both at the modiolar side and pillar side. However, the loss was much more pronounced in the IHCs' modiolar side (9.56 ± 0.5 ribbons vs 3.27 ± 0.24 ribbons; unpaired t-test p =5.57 E-10) and pillar (5.9 ± 0.6 ribbons vs 3.6 ± 0.6 ribbons, unpaired t-test p = 0.016). (**D**) The increase in volume affected both modiolar (P30=0.24 ± 0.02 μm^3 vs P365=0.7 ± 0.1 μm^3 unpaired t-test, p = 3.7 E-11) and pillar (P30= 0.12 ± 0.01 μm^3 vs P365= 0.57 ± 0.07 μm^3, unpaired t-test p = 7.5 E-14) synaptic ribbons.
This comparative analysis was performed in IHCs of the mid-cochlear region (encoding 8-16 kHz).

Postsynaptic afferent endings to ribbon IHCs express AMPA-type ionotropic glutamate [glutamate receptor A2 (GluA2)]-containing AMPA receptors (Matsubara et al., 1996; Hu et al., 2020). To determine whether the organization of postsynaptic AMPARs facing the IHCs ribbon was modified in old P365 mice we performed GluA2 immunostaining and confocal fluorescence imaging (Fig.5). As compared to young ribbon synapses, old synapses had larger ribbons associated with larger AMPAR clusters, suggesting that the changes occurring with aging are both at the pre and postsynaptic side in good agreement with the EM morphological analysis of Stamataki et al. (2006).

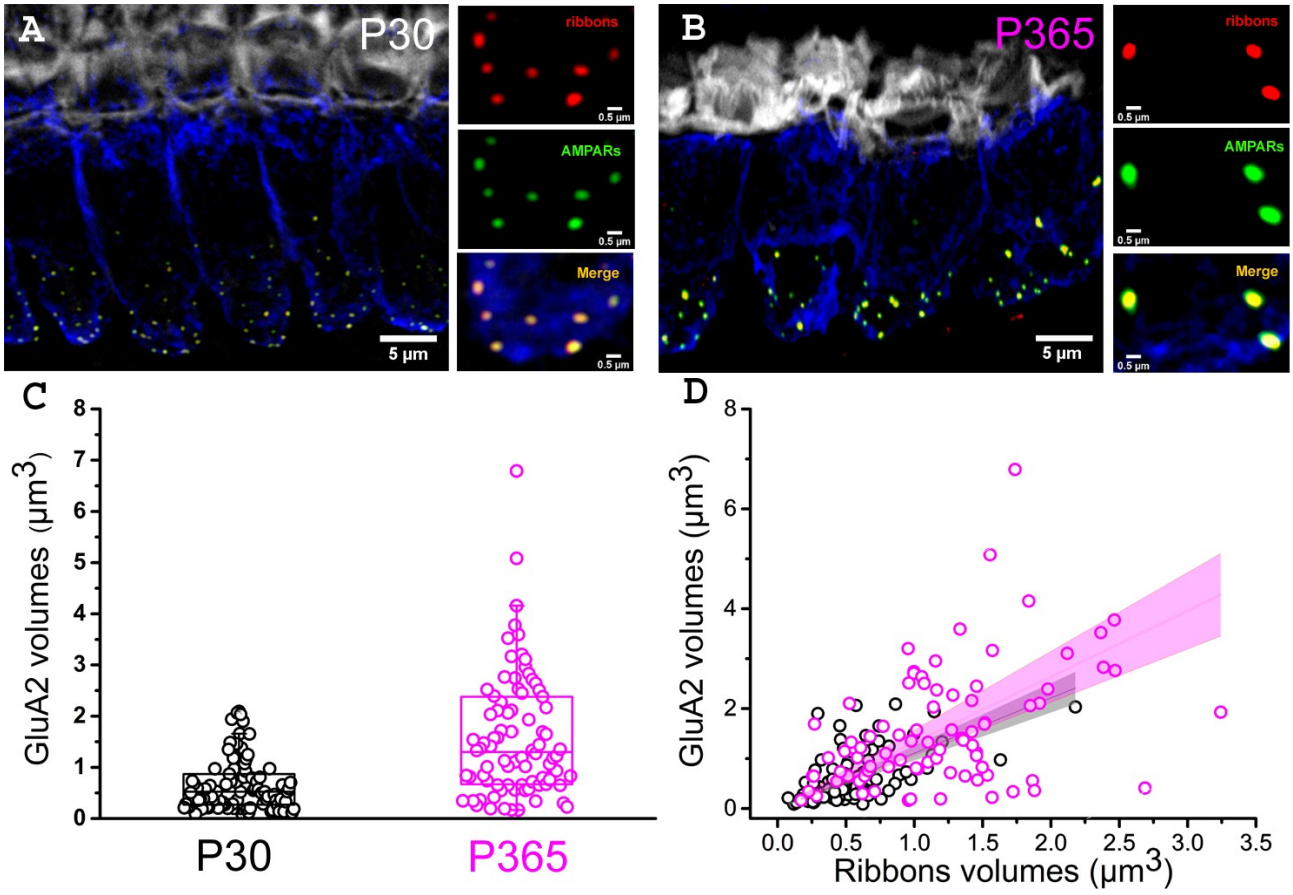

Figure 5. Larger postsynaptic patches of GluA2 receptors in old IHCs. (**A to D**) Immuno-confocal imaging of IHCs (stack reconstructions of 22 slices of 0.3µm thickness) showing otoferlin (blue), the synaptic ribbons (Ribeye/CtBP2, red dots) and the post-synaptic AMPA receptors (GluA2, green dots). Fluorescent-phaloidin (grey) labelled F-actin in the strereocilia The white bars indicate 5 µm in A and B, then 0.5µm in C and D. (**C**) Comparative distribution of the volume of postsynaptic patches of AMPA GluA2 receptors. Note that the GluA2 receptor volume significantly increased with aging in C57Bl/6J mice ($p < 0.001$; unpaired-t test); (n = 86 synapses; from 3 mice at P30 (16 IHCs) and P365 (29 IHCs) ; mid-cochlear region encoding 8-16 kHz). (**D**) Comparative volume distribution of postsynaptic GluA2 and corresponding postsynaptic ribbon in P30 and P365 IHCs. Note a good linear correlation between GluA2 and ribbon volumes (Pearson's coefficient r = 0.93 and 0.86, respectively for P30 and P360).

Drastic IHC cell size reduction wih aging

To determine whether the loss of synaptic ribbons was associated with a cell size reduction in old P365 IHCs, we labeled the cytosol of IHCs with an antibody against myo-7a, an unconventional myosin essential for the hair bundle functional integrity and found in the apical sterocilia as well as the cytoplasm of the hair cells (Hasson et al., 1995). We found a drastic reduction of the basal infra-nuclear synaptic zone of the IHCs from an average of 15.7 ± 0.1 µm (n=34) in P21 IHCs to 12.4 ± 0.3 µm (n=50) in old P365 IHCs (unpaired-t test, p = 1.1 E-13), Fig. 6A-C). The cell size reduction of old IHCs was confirmed by another method using whole-cell patch clamp measurement of the IHC resting membrane capacitance in organs of Corti preparation ex-vivo (Fig.6D-E). P365 IHCs displayed a significant smaller resting capacitance, measured at -70 mV, of 7.9 ± 0.4 pF (n=22) as compared to P21 IHCs (10. 8 ± 0.1 pF, n=44, unpaired t-test, p = 3.7 E-10).

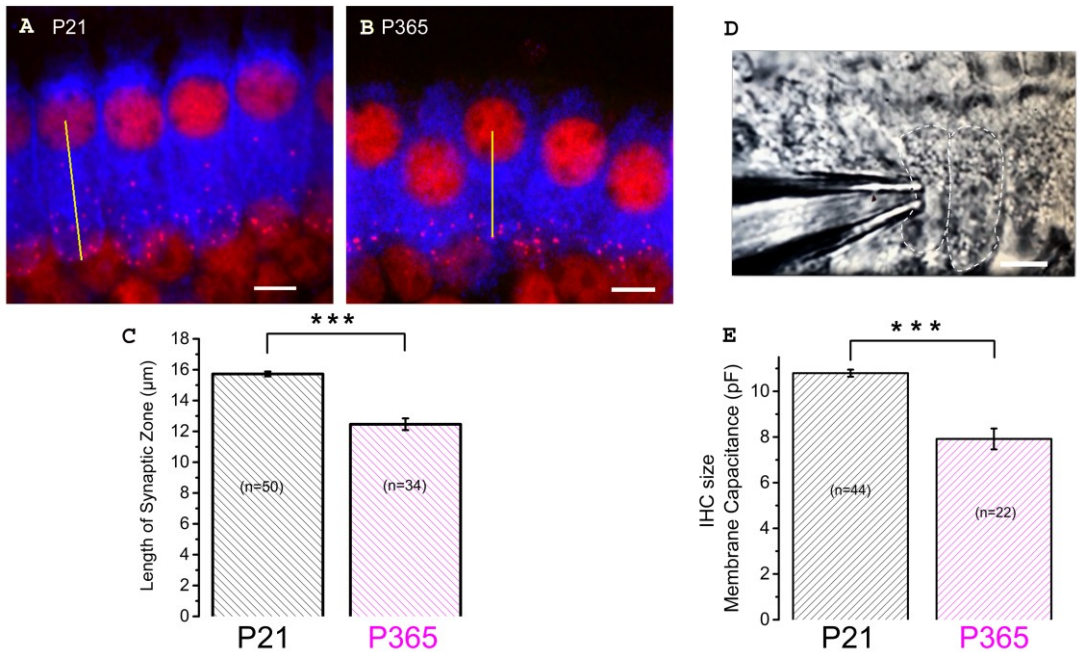

Figure 6. Cell size reduction of IHCs with aging. (A-B) Immuno-confocal imaging of IHCs labeled for myo-7a (blue) and CtBP2 (labeling the ribbons, red) in P21 (A) et P365 (B) mice (reconstructed stack images of 22 slices of 0.3 µm thick). The length of the infra-nuclear synaptic zone was measured from the center of the nucleus to the bottom of the cell as indicated by the yellow line. The scale bar indicated 5 µm. (C) Comparative histogram of the length of the infra-nuclear synaptic zone. Asterisks indicated statistical significance with p < 0.0001, unpaired t-test.) Measurements were made from IHCs of the mid-cochlear region (8-16 kHz). (D) Photomicrograph showing a row of IHCs in an ex-vivo organ of Corti explant and a patch-clamp recording electrode allowing measurements of capacitive and ionic currents. (E) Comparative mean IHC resting membrane capacitance, measured at -70 mV, in whole-cell patch-clamp configuration. Asterisks indicated values with significant difference with p < 0.0001, unpaired-t test.

Higher Ca^{2+} current density and exocytosis in old IHCs

Although the loss of IHC ribbon synapses in C57BL/6J mice with aging is well documented in the literature (see Wan and Corfas, 2015), the functional changes of the remaining "old" IHC ribbon synapses has not yet been explored in detail at the cellular level. We investigated here the changes in the calcium-evoked exocytotic responses of aging IHCs from ex-vivo explants of the organ of Corti from aging C57BL/6J mice. We recall that Ca^{2+} is a key messenger for normal hearing since it tunes the transduction of the analogic sound signal into nerve impulses. This transduction occurs at the IHC synaptic active zone through the voltage-activation of $Ca_v1.3$ Ca^{2+} channels (Brandt et al., 2003; Vincent et al., 2017) and the action of the Ca^{2+} sensor otoferlin (Roux et al., 2006; Beurg et al., 2010; Michalski et al., 2017). Increase in the density of L-type Ca^{2+} channels has long been recognized as a characteristic of aging central neurons (Thibault and Landfield, 1996; Campbell et al., 1996) but possible altered function in Ca^{2+} signaling has not been investigated in aging IHCs.

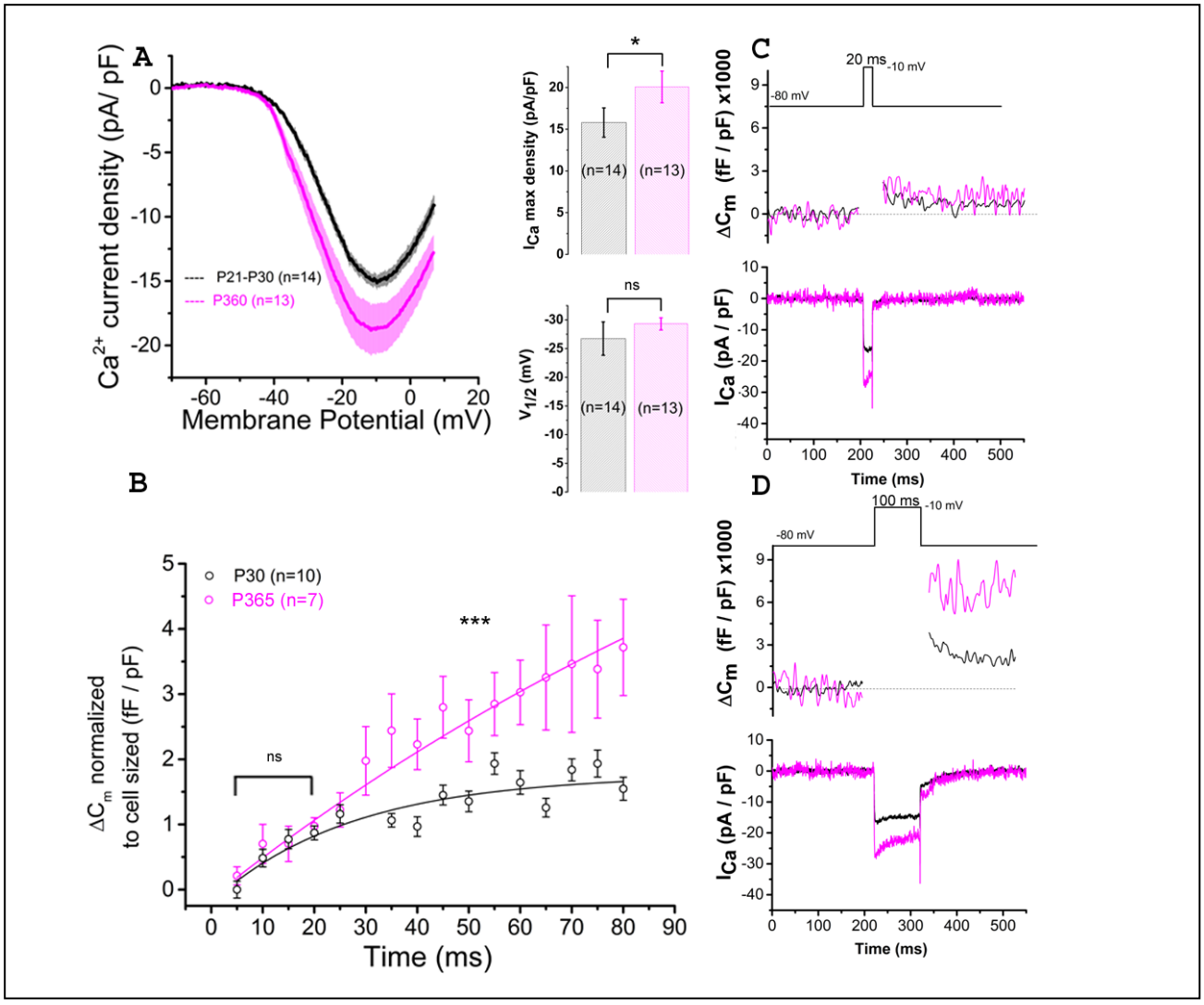

Figure 7. Ca^{2+} currents and exocytosis are exacerbated in IHCs from aged C57BL6/J mice. (**A**) Ca^{2+} current density of old P365 IHCs (pink) was larger as compared to young mature P21 IHCs (black). IHCs were subjected to a voltage ramp stimulation from -90 mV to +30 mV in 120 ms, giving a slope change in voltage of 1mV/ms. Comparative I_{Ca} maximum density measured at -10 mV indicated a significant increase in P360 IHCs (unpaired two-sample t-test, p=0.03) while the half-max voltage activation ($V_{1/2}$) of the Ca^{2+} currents remained unchanged (unpaired t-test, p = 0.06). (**B**) Kinetics of exocytosis were evoked by a voltage-steps from -80 mV to -10 mV with increasing duration from 5 ms to 80 ms. Note that brief stimulations below 25 ms, a time-frame addressing the release of the Readily Releasable Pool of vesicles, the exocytotic response (normalized to cell size) was similar in P30 and P360 IHCs (p = 0.2; two-way ANOVA). Longer stimulations, above 30 ms, which probed the activation of the secondarily releasable pool of vesicles, showed a significant increase in exocytosis (two-way ANOVA; p = 2.3 E-8), indicating that old IHCs were more likely to sustain high rates of vesicular release. (**C-D**) Representative examples of ΔC_m and $I_{Ca^{2+}}$ recordings from P30 and P365 IHCs during a 20 ms and a 100 ms voltage-step stimulation from -80 mV to -10 mV. The number of IHCs, indicated in graph, were obtained from 5 mice at P365 and 6 mice at P30.

In the present study, whole cell patch-clamp recordings from old P365 IHCs showed a significantly increase in Ca^{2+} current density (Ca^{2+} current amplitude normalized to cell size) as compared to young mature P30 IHCs, rising from a mean peak value of 15.8 ± 1.75 pA/pF to 20.1 ± 1.9 pA/pF at -10 mV (Fig. 7A; unpaired t-test, $p < 0.05$). The voltage-activation curve of the Ca^{2+} currents in old P365 IHCs remained similar to the young mature P30 IHCs, with a mean half-voltage activation ($V_{1/2}$) of -29.3 ± 1.1 and -26.7 ± 2.8 mV, respectively (unpaired t-test, p = 0.06).

Patch-clamp measurement of membrane capacitance upon depolarizing voltage-steps from -80 to -10 mV with increasing time duration allowed to compare the kinetics of vesicle exocytosis in young and old IHCs. For brief stimulations below 25 ms, a time-frame addressing the release of the Readily Releasable Pool (RRP) of vesicles, the exocytosis response (normalized to cell size) was similar in P30 and P365 IHCs (Fig. 7B-C). However, longer depolarization above 25 ms revealed a more sustained exocytotic response in old IHCs, suggesting the mobilization of a more efficient secondarily releasable pool (SRP), i.e. a more efficient vesicle recruitment in these cells. To investigate whether this increased SRP exocytosis was due to higher Ca^{2+} microdomains at the ribbon active zones, we used the high affinity Ca^{2+}-indicator Rhod-2 (K_d = 570 nM) which is known to allow a good monitoring of low Ca^{2+} concentrations ranging from 20 nM to 20 µM (Del Nido et al., 1998). We choose to use Rhod-2 rather than a low affinity Ca^{2+} dye such as OGB-5N with a Kd at 20 µM (Vincent et al., 2014) because we wanted here to primarily probe the amplitude of the Ca^{2+} microdomains, where the changes in Ca^{2+} concentrations are due to Ca^{2+} diffusion and are lower than at the nanodomain range near the Ca^{2+} channels. Ca^{2+} microdomains allow vesicle replenishment, a process occurring at the µm scale away from the ribbon and their associated Ca^{2+} channels (Spassova et al., 2004; Johnson et al., 2005; Graydon et al., 2011). We found

that, upon 5 consecutive long 100 ms voltage-step stimulations (from -80 mV to -10 mV), IHCs displayed brighter transient Ca^{2+} hot spots (measured in 1µm^2 areas) at their basal synaptic area in P365 mice as compared to young P30 IHCs (Fig. 8A-B). This indicated the expression of synaptic Ca^{2+} microdomains with larger amplitude in old P365 IHCs, a response likely due a larger Ca^{2+} channel density at their ribbon active zones (Fig. 7A). Simultaneously, in the same cells, the application of the 5 consecutive 100 ms stimulations, generated a facilitated vesicular recruitment in old P365 IHCs (Fig.8D). Also as a consequence of increased Ca^{2+} microdomains in old IHCs, the simultaneous recording of Ca^{2+} currents showed an enhanced time-inactivation, indicative of an increased Ca^{2+}-dependent inactivation due to higher intracellular Ca^{2+} concentration (Fig. 8C).

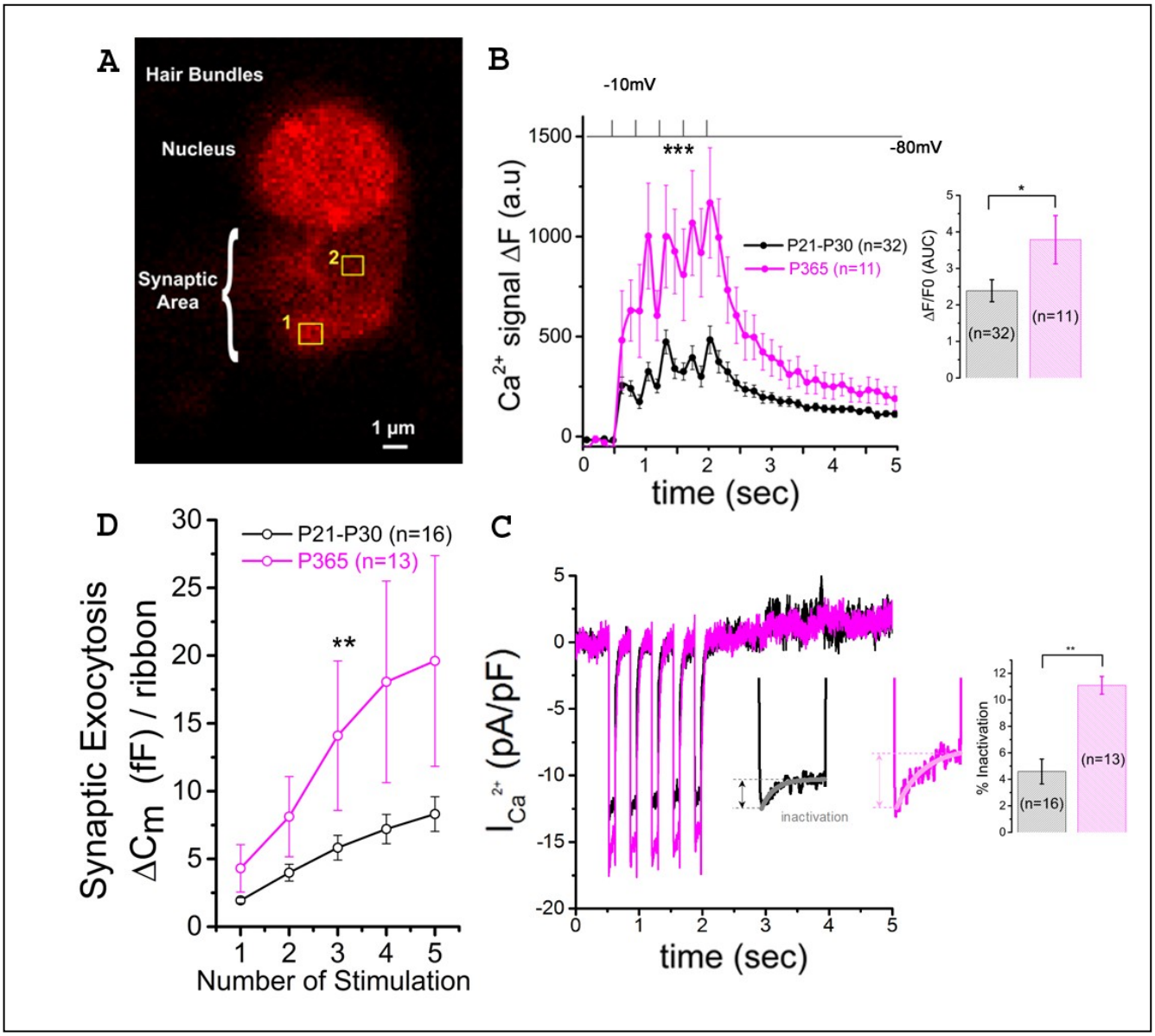

Figure 8. Larger synaptic Ca^{2+} signaling and increased sustained exocytosis in aged IHCs. (**A**) Example of confocal Ca^{2+} imaging, using the intracellular fluorescent Ca^{2+} indicator Rhod2, in an IHC. The cell was voltage-clamped at -80 mV and stimulated by 5 (100 ms) consecutive voltage-step to -10 mV. The photograph show two examples of square zones (1µm^2) below the cell nucleus where voltage-induced calcium increase was measured. (**B**) Comparative mean amplitude of transient fluorescent hot spots showed higher Ca2+ responses at the presynaptic active zones of old P365 IHCs (pink) as compared to young mature P30 IHCs (black). Hair cells were depolarized by 5 five consecutive 100 ms depolarizing steps from -80 mV to -10 mV. The values n in the graph indicated the number of active zones analyzed for young (6 IHCs from 6 mice) and old mice (5 IHCs from 5 mice), respectively. The peak of the 5 calcium responses ($\triangle F=F-F_0$ with F_0 as the fluorescent base line value averaged 0.5 s before stimulation) were significantly larger in old IHCs (two-way ANOVA (p = 8.8 E-5). The histogram compared the overall fluorescent response $\triangle F/F_0$ occurring during the 5 stimulations (0.5 to 2.5 s). The integral of the Ca^{2+} response (Area Under the Curve, AUC) was significantly larger in old P365 IHCs (unpaired t-test, p = 0.03). (**C**) Comparative mean of calcium current recorded at the same time during the 5 stimulations shown in B. Note that the inactivating part of the calcium current is increased in P365 IHCs. Asterisk indicate statistical analysis with unpaired t-test. (**D**) The concomitant exocytosis was also measured during the 5 stimulations shown in B Exocytosis measured as the variation of membrane capacitance was normalized for each IHC to their ribbon number or cell size; both normalization giving similar results). The exocytotic responses were larger in old P365 IHCs. The asterisks indicated statistical significant difference with p<0.05 (two-way ANOVA; p = 0.0015).

Aging promoted autophagy in IHCs through the recruitment of LC3B

The size reduction of the old IHCs (Fig.6) suggested that the degenerative process of the ribbon synapses was associated with a concomitant reduction of the cell surface membrane of IHCs during aging, suggesting a largely augmented uptake of plasma membrane through endocytosis. Like other type of cells, such as neurons or retinal cells, auditory hair cells utilize autophagic pathways to maintain cell homeostasis during excessive ROS production (Defourny et al., 2019; Fu et al., 2018). Autophagy is a degradation process where cytoplasmic and plasma membrane components are engulfed by vesicles called autophagosomes. To determine whether this process could explain the IHC size reduction with aging, we investigated the recruitment of LC3B, a structural protein of autophagosomal membranes. We assessed and compared the autophagosome numbers and surface area in young P30 and old P365 IHCs by quantifying LC3B puncta numbers/cell by using confocal immunofluoresence. We found that the number and overall surface area of LC3-positive structures in IHCs largely increased with aging (Fig.9), indicating an increased autophagosome formation. Similar investigations in P365 CBA/J mice, a strain which does not display early age-related hearing loss (Fig. 1), showed a weak expression of LC3B in IHCs (Fig. 9).

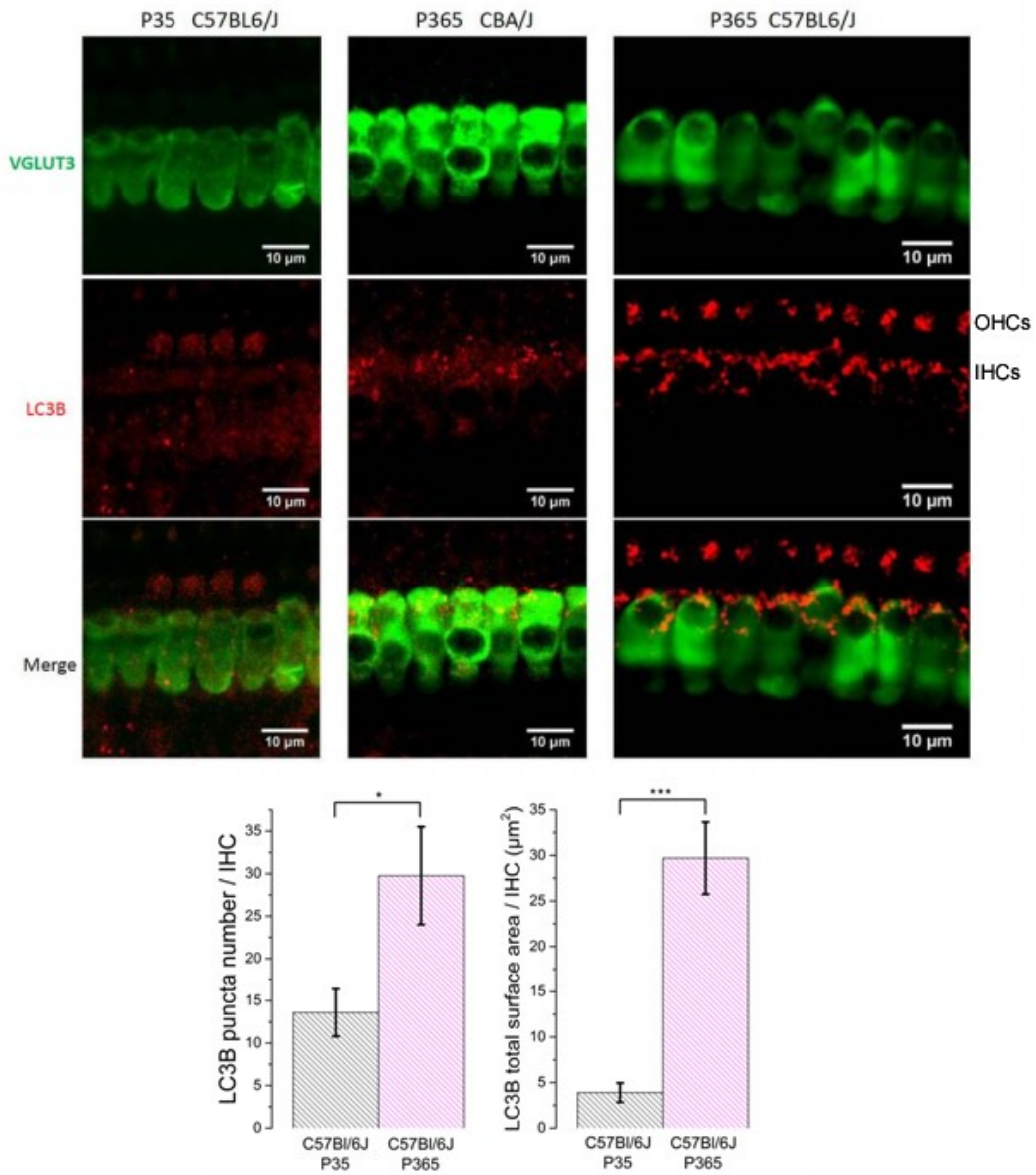

Figure 9. LC3-positive structures are prominent in aging IHCs. Representative confocal immunofluorescence images showing LC3B staining in IHCs from young P30 C57BL/6J (left), old P365 CBA/J (middle) and old P365 C57BL/6J (right) mice.The histograms below show the quantification of the LC3B puncta average number and average mean surface area per IHC. Images were obtained from processing confocal stack images (22 of 0.3 µm thickness) using ImageJ quantification tool (3D-object counter). Quantification was performed from 25 to 30 IHCs for each condition in the mid-cochlea (encoding region 8-16 kHz; 3 mice). Asterisks indicate statistical significance $p < 0.05$ (unpaired t test).

Clustering and voltage-dependent activation of BK channels are affected aging in IHCs

There is increasing evidence that oxydative damage due to an increase in ROS levels plays a crucial role in age-related degeneration of the synaptic ribbon synapses (Fu et al., 2018; Rousset et al., 2020). BK ($K_{Ca1.1}$) channels are known to be highly sensitive to oxydative stress and their activity is a good indicator of intracellular ROS production (Sahoo et al.,

2014; Hermann et al., 2015). Interestingly, a decrease in BK channel expression in IHCs has been associated to noise-related ROS and peroxysome pathology (Delmaghani et al., 2015) but never yet described in IHCs during age-relate hearing loss. It is worth recalling that BK channels allows fast repolarization of IHCs and are essential for phase-locking of the auditory afferent neurons (Kros et al., 1998; Skinner et al., 2003; Oliver et al., 2006; Kurt et al., 2012). We here investigated, using immunofluorescent confocal microscopy, the comparative level expression of BK channels in IHCs from young (P30) and old P365 C57BL/6J mice. In young mature IHCs, BK channels are known to be organized in a dozen of clusters at the neck of the IHCs below the cuticular plate (Pyott et al., 2004; Hafidi et al., 2005). We used 3-D reconstructions from stacks of confocal images of immunostained organs of Corti (mid-cochlear frequency region 8-16 kHz) to determine the mean total surface area of the BK clusters per IHCs (Fig.10A-C). The results indicated that the membrane surface covered by BK channel clusters was reduced almost three fold in P365 IHCs as compared to P30 IHCs.

To further characterize the changes in BK channel function with aging, we performed whole cell patch-clamp recordings in IHCs from P30 and P365 mice. Since BK currents in IHCs have the peculiar property to be extremely fast activating currents (also termed IK_f; Kros et al., 1998), these currents were recorded during brief 20 ms depolarizing steps and measured 2.5 ms after their onset (Fig.10D-F). BK currents in IHCs from young mature have also the particularity to activate at extremely negative membrane potential (near -60 mV) (Lingle et al., 2019). While the whole-cell conductance of BK channels from P365 IHCs was not significantly different from P30 IHCs (0.26 .± 0.04 nS and 0.23 ±.0.03 nS, respectively), their voltage-dependant activation showed a large positive shift of 7 mV (Fig.10F). Interestingly, the decrease in size of the BK patches and the positive voltage-activation shift in old IHCs somewhat resembled the phenotype observed in mice KO for LRRC52, a γ BK regulatory subunits (Lang et al., 2019; Lingle et al., 2019), suggesting that the BK complex formed with this γ subunit could be one the target of the degenerative oxydative process in aging C57BL56/J mice IHCs.

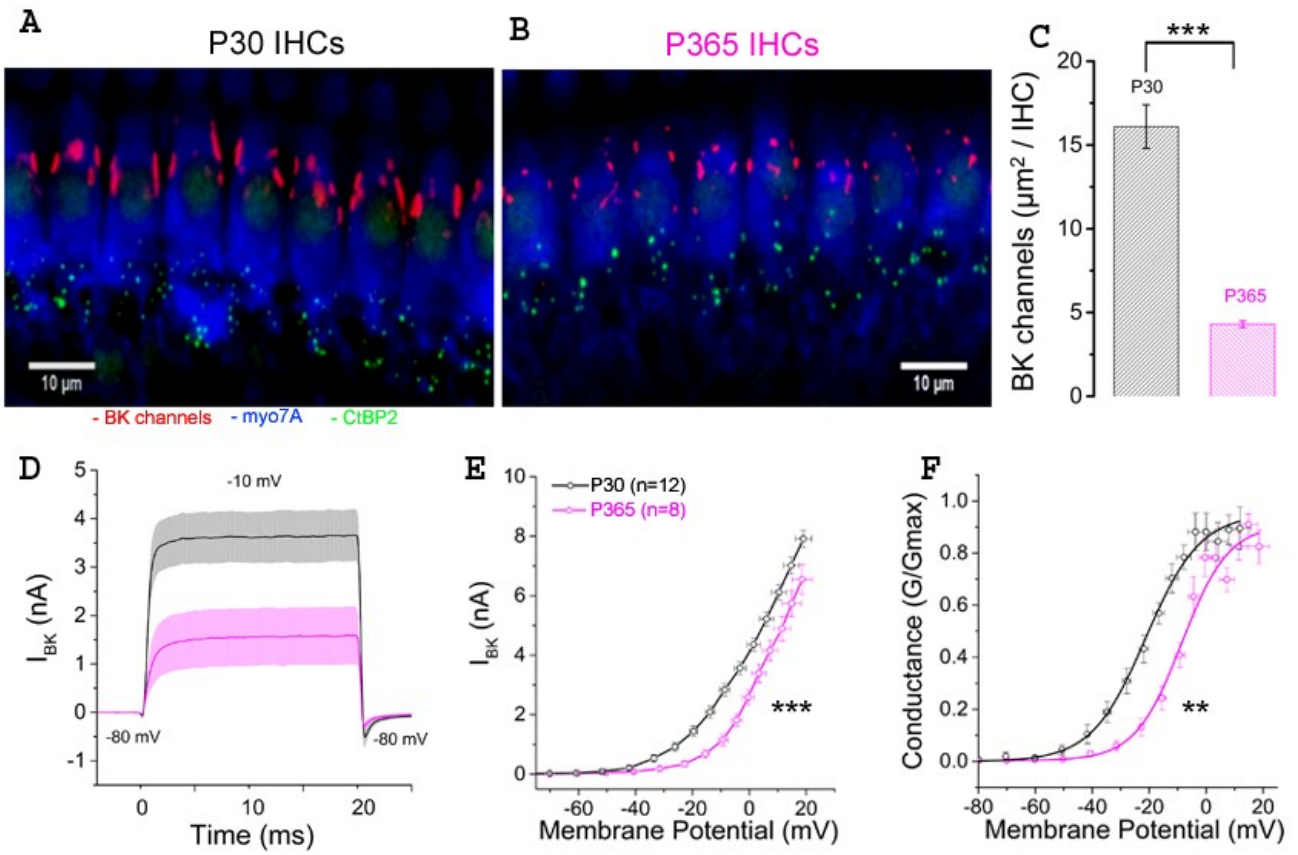

Figure 10. Immunofluorescent confocal imaging of BK channels in aging IHCs. (**A**) Numerous large BK channel clusters (red) are localized extrasynaptically below the cuticular plate of IHCs in young mature P30 C57BL6/J mice. (B) Note the strong reduction in size of the BK channels clusters in IHCs of old P365 C57BL6/J mice.
(**C**) Histogram comparing the total surface area covered by the BK channel clusters per IHC in the mid-turn cochlea (region encoding 8-16 kHz). The total number of IHCs analyzed was 58 and 25 from P30 (n=3) and P365 (n=3) mice, respectively. Asterisks indicate statistical significance with $p<0.05$ ($p = 1.12$ E-7; unpaired t test).
(**D**) Comparative fast outward potassium currents (IKf), carried by BK channels, recorded from P30 (black, n=12) and P360 (pink, n=8) IHCs when using a brief depolarization step of 20 ms from -80 to -10 mV.
(**E**) Comparative BK current-voltage curves (n = 12 and 8 IHCs respectively in P30 and P360 mice, from 3 mice at each age). Significantly different two-way ANOVA, $p = 2.7$ E-8. IKf was measured 2.5 ms after the onset of the voltage-step stimulation. (**F**) Comparative BK conductance fitted with a Boltzmann curve indicated a V1/2 of -20.5 ± 5.7mV in P30 IHCs and of -13.7 ± 1.4 mV in P365 IHCs, respectively (unpaired t-test, $p = 0.009$). Note that voltage error across series resistance (Rs = 5 ± 2 MΩ) and leak current were compensated for each IHC. All values are expressed as means ± SEM.

DISCUSSION

Larger synaptic ribbons associated with increased Ca^{2+} signals

Ribbons are presynaptic organelles tethering glutamate-filled vesicles at the hair cell active zone (AZ). These intracellular structures, composed of the protein RIBEYE, are anchored by

475 the scaffold protein bassoon to the AZ plasma membrane, adjacent to Ca^{2+} $Ca_V1.3$ channels
476 (Brandt et al, 2003; Graydon et al., 2011; Jing et al., 2013; Vincent et al., 2017). Ribbons are
477 essential for high rate of transmitter release and for high temporal precision of neuronal
478 encoding of sound at the auditory afferent nerve fibers (Jean et al., 2018; Becker et al., 2018).
479 Each auditory IHC have 10 to 20 synaptic ribbons depending of their cochlear frequency
480 location (Meyer et al., 2009). Ribbons are heterogeneous in size and each ribbon makes a
481 single synaptic contact with one afferent nerve fiber. Remarkably, fibers associated to large
482 ribbons display low spontaneous rate and high-threshold have the tendency to be distributed
483 at the modiolar side of IHCs (Liberman et al., 2011). Nerve fibers associated with smaller
484 ribbons display high spontaneous rate and low-threshold activation, are mainly located toward
485 the pillar side of IHCs. Interestingly, we found here that old C57BL6/J IHCs preferentially
486 loose modiolar ribbons (known to be associated with high threshold low spontaneous fibers),
487 therefore mimicking what is happening during noise-induced hearing loss (Fernandez et al.,
488 2015; Liberman and Kujawa 2017; Hickman et al., 2020). Heterogeneity in the voltage-
489 dependence of Ca^{2+} channels and release site coupling has been recently proposed to
490 contribute to the firing fiber specificity, with modiolar ribbons being activated at more
491 negative potentials (Özçete and Moser 2021). In our study, we did not find evidence for a
492 voltage-shift in the voltage-dependence of Ca^{2+} channels with aging but we did observe an
493 increase in the density of Ca^{2+} currents. The increase in Ca^{2+} entry was further confirmed by
494 the stronger time-inactivation of the Ca^{2+} currents (Grant and Fuchs, 2008; Vincent et al.,
495 2017).
496 One of the most striking observations was that the IHC synaptic ribbons underwent a nearly
497 threefold increase in size with aging, confirming a certain degree of plasticity of these
498 synaptic structures. The enlargement of the presynaptic ribbons was in good agreement with a
499 previous ultrastructural study in aging C57BL/6J mice by Stamataki et al. (2006) and the
500 recent study of Jeng et al., (2020). Interestingly, the size of the young mature IHC synaptic
501 ribbons is known to correlate positively with the AZ Ca^{2+} microdomain amplitude, as well as
502 the number and gating of the $Ca_v1.3$ Ca^{2+} channels (Frank et al., 2009; Neef et al., 2018).
503 Also, hair cells of transgenic zebrafish with enlarged ribbons display larger ribbon-localized
504 Ca^{2+} currents (Sheets et al., 2017). In agreement with these previous studies, we found here,
505 in IHCs from aging C57BL/6J mice, that the remaining larger ribbons were associated with
506 larger Ca^{2+} microdomain amplitude, and larger density of calcium currents, reinforcing the
507 idea that Ca^{2+} ions regulate the size of the synaptic ribbons. In this context, It is worth

recalling that mitochondrial-Ca^{2+} uptake has been proposed to lower cellular NAD^+/NADH redox and regulates ribbon size, possibly by acting through the NAD^+ binding site of the B domain of RIBEYE (Wong et al., 2019). In vitro work has shown that NAD^+ and NADH can promote interactions between ribeye domains (Magupalli et al., 2008) and the size of the ribbons would be then sensitive to the subcellular synaptic NAD^+/NADH redox level (Wong et al., 2019), suggesting that the increase in size of the IHCs ribbons from aged C57BL/6J mice also results from NAD^+/NADH homeostasis disruption.

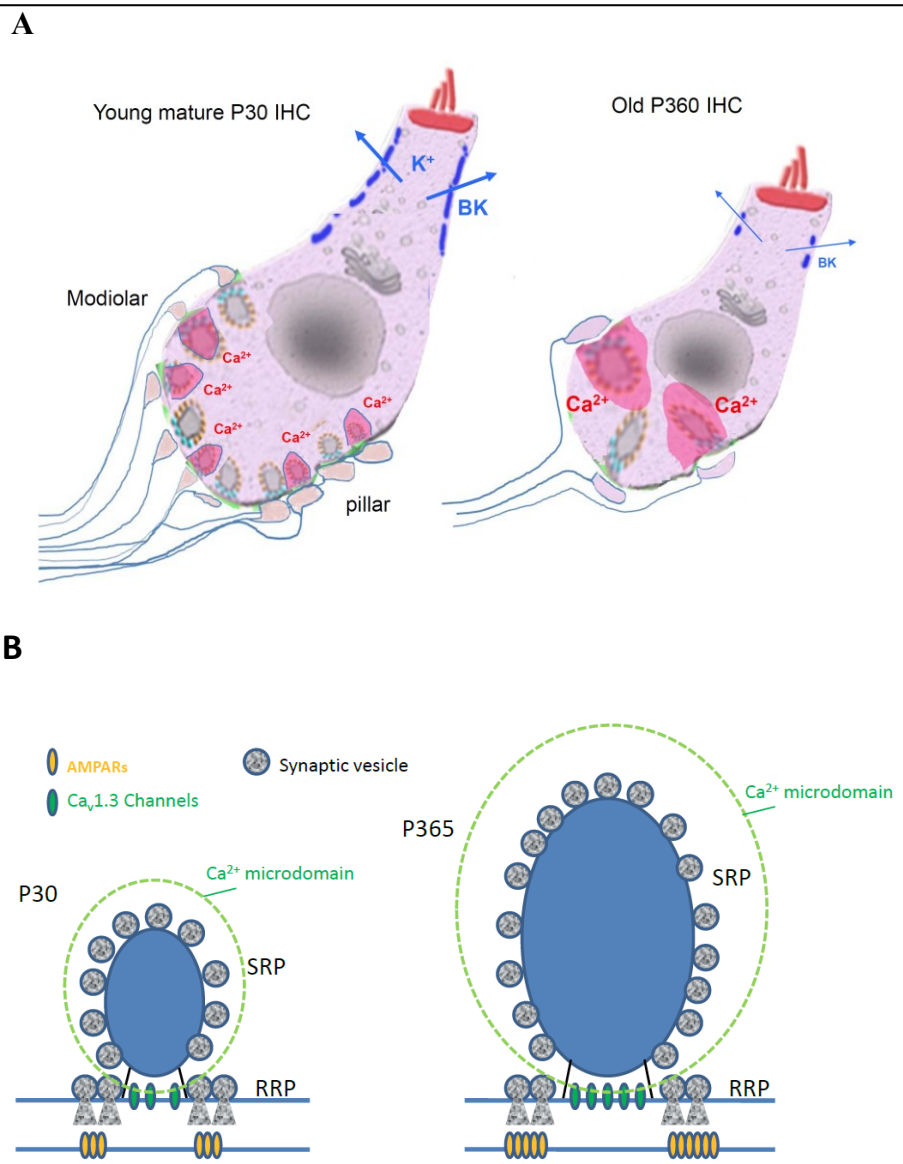

Figure 11. Synaptic IHC degeneration was associated with a strong potentiation of the remaining ribbon synapses in aging C57BL/6J mice. (**A**) Age-related hearing loss in P360 mice was associated with IHC shrinkage (cell size reduction), an important loss of afferent ribbon synapses (>50%), a drastic enlargement of the surviving synaptic ribbons (both at pillar and modiolar side), an increase in Ca^{2+} signaling (larger Ca^{2+} microdomain amplitude as indicated by the larger pink domains around the ribbons) and a large decrease in the fast repolarizing BK channel clusters (blue bars). (**B**) Hypothetical view of a young and old IHC ribbon synapse.

524 **Increased capacity for sustained IHC synaptic exocytosis: Implication for the discharge**
525 **pattern of the auditory nerve firing**
526 As a consequence of larger Ca^{2+} microdomains, we found that IHCs from old C57BL/6J mice
527 had larger and more sustained exocytotic responses. These larger release responses could also
528 well be explained by a higher synaptic vesicle density at the active zone of the IHC ribbon
529 synapses as suggested by the EM study of Stamataki et al. (2006). Surprisingly, the recent
530 study of Jeng et al., (2020), which did not perform Ca^{2+} imaging, concluded that the size and
531 kinetics of Ca^{2+}-dependent exocytosis in IHCs were unaffected in aging mice but this study
532 did not normalize the IHC exocytotic responses to their cell size or to their ribbon synapse
533 number, and therefore may have overlooked the differential phenotype.
534 What would be the consequences on the discharge pattern of the remaining afferent fibers of a
535 more sustained release capacity in old ribbon synapses ? Fast adaptation in the discharge rate
536 of the afferent auditory nerve fibers is thought to be one of their essential property for
537 emphasizing the timing information of sound stimuli. This adaption takes the form of a fast
538 increase in spike rate at stimulus onset that rapidly declines in a double exponential decay to a
539 lower steady-state rate after a few tens of milliseconds (Taberner and Liberman 2005). The
540 origin of this fast adaptation has been proposed to arise first from H^+ release block of Ca^{2+}
541 channels and second to rapid depletion of synaptic vesicle release (Vincent et al., 2017). We
542 predict that the increased capacity to sustain SRP exocytosis in old IHCs with larger ribbons
543 would have the tendency to decrease the level of firing adaptation of the auditory fibers and
544 therefore explain the altered recovery from short-term adaptation in old C57BL/6J mice
545 (Walton et al., 1995).
546 Furthermore, we confirmed here the hyperacusis-like effect of the startle responses in old
547 C57BL/6J mice (Ison et al., 2007). This increased response at low sound intensity could be
548 explained by a release potentiation at the IHC ribbon synapses due to the presynaptic higher
549 Ca^{2+} channel density associated with a larger ribbon coupled with a larger vesicular SRP, and
550 increased expression of post-synaptic AMPARs. All these features would make the auditory
551 ribbon synapses hypersensitive and underlie the hyperacusis-like reflex in old C57BL/6J
552 mice.
553
554 **IHC shrinkage and disruption of BK channel clusters**
555 Another novel observation of our study was the drastic reduction in cell size of IHCs from
556 aging C57BL/6J mice. Interestingly, tuberous sclerosis rapamycin-sensitive complex 1

557 (mTORC1) has been shown to be overactivated and promote oxidative damages to synapse
558 ribbon loss in aging C57BL/6 mice (Fu et al., 2018). We found that aged P365 IHCs had an
559 increase expression of the autophagy marker LC3B. The activation of the mTOR pathway
560 with aging could therefore trigger the cell size reduction of IHCs, by activating the autophagy
561 pathway, as proposed in many other cell types (Fingar et al., 2002; Fumarola et al., 2005). In
562 addition, our study described another novel remarkable feature of aging IHCs, a drastic
563 disruption of the BK channel clusters, suggesting that these potassium channels are also a
564 good indicator of the redox state and autophagy in IHCs. The expression and distribution of
565 BK channels could be regulated through the rapamycin insensitive mTOR complex 2
566 (mTORC2) as shown in the kidney glomerulus podocytes (Wang et al., 2019). Interestingly,
567 the disruption of the BK channel clusters in aging IHCs was associated with a large positive
568 shift in their voltage-activation curve, suggesting that the fast repolarizing property mediated
569 by BK channels which likely contributes to decrease transmitter release (Skinner et al., 2003),
570 would be largely hampered during sound stimuli in aging mice, an additional factor that may
571 also contribute to hyperacusis.
572

573 ## CONCLUSIONS

574 In conclusion, our study unraveled several novel functional and structural features of aging in
575 IHC ribbon synapses from C57BL/6J mice (Fig.10): 1) a large reduction in IHC cell size, 2) a
576 drastic enlargement of the presynaptic ribbons and postsynaptic AMPAR clusters 3) an
577 increased presynaptic Ca^{2+} signaling associated with a stronger sustained exocytotic response
578 4) a disruption of BK channel clusters and a drastic shift in their voltage-dependence
579 decreasing their potential negative feedback on neurotransmission. Overall, these results
580 suggested that aging IHCs ribbon synapses can undergo important structural and functional
581 plasticity that lead to synaptic potentiation that could explain the paradoxical hyperacusis-like
582 exaggeration of the acoustic startlle reflex observed in C57BL/6 mice.
583

584 ## MATERIALS and METHODS

585 ### Mice

586 Inbred C57BL/6J mice, which are homozygous for the recessive cadherin23 mutation
587 *Cdh23*^{753A} (also known as Ah1) were used in the present study. Hearing thresholds and IHC
588 ribbon counts in mice of either sex were performed at postnatal ages: P15, P30, P60, P180

589 and P365. CBA/J mice (from Charles River) were also tested as controls at P50, P250 and
590 P365. Animal care and all procedures were approved by the institutional care and use
591 committee of the University of Bordeaux and the French Ministry of Agriculture (agreement
592 C33-063-075).
593
594 **Assessment of hearing thresholds (ABRs)**
595 To record ABRs (Auditory Brainstem Responses, which represent the sound-evoked
596 synchronous firing of the auditory cochlear nerve fibers and the activation of the subsequent
597 central auditory relays), mice were anesthetized with intraperitoneal injection of xylazine (6
598 mg/ml, Rompun Bayer) and ketamine (80 mg/ml, Virbac) mixture diluted in physiological
599 saline. The mouse was placed in a closed acoustic chamber and its body temperature was kept
600 constant at 37°C during ABRs recording. For sound stimulus generation and data acquisition,
601 we used a TDT RZ6/BioSigRZ system (Tucker-Davis Technologies). Click-based ABR
602 signals were averaged after the presentation of a series of 512 stimulations. Thresholds were
603 defined as the lowest stimulus for recognizable wave-I and II. The amplitude of ABR wave-I
604 was estimated by measuring the voltage difference between the positive (P1) and negative
605 (N1) peak of wave-I. Sound intensities of 10 to 90 dB SPL in 10 dB step, were tested.
606 Distortion product otoacoustic emissions (DPOAEs), which originate from the
607 electromechanical activity of the outer hair cells (OHCs), were tested by using two
608 simultaneous continuous pure tones with frequency ratio of 1.2 (f1 = 12.73 kHz and f2 =
609 15,26 kHz). DPOAEs were collected with the TDT RZ6/BioSigRZ system designed to
610 measure the level of the "cubic difference tone" 2f1-f2.
611
612 **Acoustic Startle Reflex (ASRs) measurements**
613 Testing was conducted in four acoustic startle chambers for mice (SR-LAB, San Diego
614 Instruments, San Diego, CA). Each chamber consisted of a nonrestrictive cylindrical
615 enclosure attached horizontally on a mobile platform, which was in turn resting on a solid
616 base inside a sound-attenuated isolation cubicle. A high-frequency loudspeaker mounted
617 directly above the animal enclosure inside each cubicle produced a continuous background
618 noise of 65 dBA and various acoustic stimuli in the form of white noise. Mechanical
619 vibrations caused by the startle response of the mouse were converted into analog signals by a
620 piezoelectric accelerometer attached to the platform. A total of 130 readings were taken at
621 0.5-ms intervals (i.e., spanning across 65 ms), starting at the onset of the startle stimulus. The

average amplitude over the 65 ms was used to determine the stimulus reactivity. The sensitivity of the stabilimeter was routinely calibrated to ensure consistency between chambers and across sessions.

Acoustic startle reflex was assessed during a session lasting for approximately 30 minutes, in which the mice were presented with a series of discrete pulse-alone trials of different intensities and durations. Ten pulse intensities were used: 69, 73, 77, 81, 85, 90, 95, 100, 110, and 120 dBA lasting for either 20 or 40 ms (background noise level: 65 dBA). A session began when the animals were placed into the Plexiglas enclosure. The mice were acclimatized to the apparatus for 2 minutes before the first trial began. The first six trials consisted of six pulse-alone trials of 120 dBA, comprising three trials of each duration. These trials served to stabilize the animals' startle response, and were analyzed separately. Subsequently, the animals were presented with five blocks of discrete test trials. Each block consisted of 20 pulse alone trials, one for each intensity and duration. All trials were presented in a pseudorandom order with an inter-trials interval of 14 seconds.

Tissue preparation and imunocytochemistry

Mice were deeply anesthetized with isofluorane (Vetflurane, Virbac). The ramps of the cochlear apparatus were dissected and prepared as previously described by Vincent et al. (2014). Inner ears (cochleae) were fixed by incubation in 4% paraformaldehyde in phosphate-buffered saline (PBS), pH 7.4, at 4°C overnight and washed with cold phosphate buffered saline (PBS). They were then incubated for 2 days in PBS solution containing 10% EDTA pH 7.4 at 4°C. The middle part of the organ of Corti (area encoding between 8 and 16 kHz) was then dissected and the tectorial membrane removed. The tissue was first incubated with PBS containing 30% normal horse serum and triton X100 0.5 % for 1 hour at room temperature. Synaptic ribbons were labeled with anti-CtBP2 (1/200 Goat polyclonal, Santa Cruz, USA ; cat # SC-5966 or 1/200 Mouse IgG1 monoclonal antibody BD Biosciences, cat # 612044). Otoferlin was labeled with a mouse monoclonal antibody (1/200 AbCam, cat # ab53233). Autophagy was detected by labeling LC3B protein with anti Rabbit monoclonal antibody (1/200 LC3B(D11) XP, Cell Signaling Technology, cat # 3868). BK channels were labeled with a Rabbit polyclonal antibody (1/200, Alomone, Israel, cat #APC-021. Explants of Organ of Corti were incubated overnight at 4°C with primary antibodies. The following fluorescent secondary antibodies 1/500 were then used: anti-Goat Donkey polyclonal Fluoprobes 547H (Interchim, cat# FP-SB2110), anti-Mouse Donkey polyclonal Fluoprobes 647H (Interchim,

655 cat# FP-SC4110), anti-Mouse Donkey polyclonal Alexa Fluor 488 (AbCam, cat# ab150109),
656 anti-Mouse Goat polyclonal Alexa Fluor 546 (Molecular Probes, cat# A-11003), anti-Mouse
657 Goat polyclonal Alexa Fluor 488 (Molecular Probes, cat# A-10680), anti-Rabbit Donkey
658 polyclonal Fluoprobes 594 (Interchim, cat# FP-SD5110). Actin-F was also used to visualize
659 hair cells (1/100, Phalloidin Fluoprobe 405, Interchim, Montlucon, France; cat # FP-
660 CA9870). For Image Acquisition, organ of Corti samples were analyzed using a confocal
661 laser scanning microscope Leica SP8 with a 63X oil immersion objective (NA = 1.4) and
662 white light laser (470 to 670 nm) (Bordeaux Imaging Center). Phalloidin was imaged by using
663 a diode laser at 405 nm also mounted on the microscope. For complete 3D-stack
664 reconstruction of IHCs, 25 to 30 images (0.3 µm thickness) were acquired as previously
665 described (Vincent et al, 2014). Ribbon volumes were calculated using the 3D-Objects
666 Counter Plugin of ImageJ. Image resolution was 0.038 µm/pixel. As previously described by
667 Hickman et al. (2020) and Jeng et al., (2020), the x,y,z coordinates of ribbons in each z-stack
668 were transformed into a coordinate system based on the modiolar-pillar polarity of the IHCs.
669 We determined the pillar versus modiolar distribution of the synaptic ribbons by using a *k*-
670 means clustering method in the z-stack position of each ribbon, with arbitrarily choosing the
671 number of cluster as 2 (OriginPro 9.1software, OriginLab, Northampton, USA). From these 2
672 clusters, we determine arbitrarily the border between the modiolar and pillar side in each IHC
673 by taking the half-distance between the two nearest ribbon of each cluster.
674

675 **High resolution imaging of synaptic ribbons with confocal STED microscopy**

676 For high-resolution imaging of IHC ribbons, we used a Leica DMI6000 TCS SP8 STED
677 microscope with 93X glycerol immersion objective (NA 1.3) (Bordeaux Imaging Center).
678 Mouse sensory organs were fixed and incubated with primary anti CtBP2 (1/100) antibodies
679 in conditions similar to those described above for confocal microscopy. Secondary antibodies
680 Goat anti- IgG1 Mouse polyclonal Alexa Fluor 647 (Jackson, cat# 115-605-205) were used to
681 label CtBP2 primary antibodies. The pulsed STED depletion laser (pulsed laser IR, Spectra
682 Physics Mai Tai) was set at 775 nm. Stack images were acquired with the following
683 parameters: scan rate 200 Hz, 775 nm depletion laser power between 8 and 15%, scans frames
684 accumulated per *X*-*Y* section 8 times, z- step size 0.25 µm, number of plans between 8 and
685 10, pixel size 20 nm giving an *X*-*Y* image size of 21 × 5 µm (1024 × 256 pixels).

686

687 **Counting spiral ganglion neurons**

688 The afferent nerve fibers of the auditory nerve were fluorescently labeled using a retrograde
689 track tracing technique with dextran amines (Fritzsch et al., 2016). Cochleae were extracted
690 from temporal bone of freshly euthanised mice and rapidly immerged intact into ice-cold
691 artificial perilymph (NaCl 135; KCl 5.8; $CaCl_2$ 1.3; $MgCl_2$ 0.9; NaH_2PO_4 0.7; Glucose 5.6;
692 Na pyruvate 2; HEPES 10, pH 7.4, 305 mOsm). A small crystal of tetramethylrhodamine
693 dextran amines 3000 (Life technologies, NY) was placed for 15-20 min at the edge of the
694 auditory nerve coming out at the internal auditory canal of the intact cochlea and rinsed with
695 artificial perilymph. The intracochlear sensory tissues were then fixed by gentle perfusion of a
696 4% PFA solution for 30 min and rinsed with PBS. They were then decalcified for 2 days in
697 PBS solution containing 10% EDTA pH 7.4 at 4°C. The cochleae were then sliced with a
698 razor blade along the longitudinal cochlear axes and the slices were then mounted on a glass-
699 slide for fluorescent confocal microscopy observation. The quantification of the spiral
700 ganglion neurons per surface area of the neural ganglion were made in the middle part of the
701 cochlea in a region encoding 8-16 kHz, by using the 3D object counter application of ImageJ
702 software.

703

704 **Ca^{2+} currents and whole-cell membrane capacitance measurement in IHCs**

705 Measurements of resting membrane capacitance of IHCs were performed at P30 and P365
706 mice in the 20-40% normalized distance from the apex, an area coding for frequencies
707 ranging from 8 to 16 kHz, by using an EPC10 amplifier controlled by Patchmaster pulse
708 software (HEKA Elektronik, Germany), as previously described in detail (Vincent et al.,
709 2014, 2015). The organ of Corti was incubated in an extracellular perilymph-like solution
710 containing NaCl 135; KCl 5.8; $CaCl_2$ 5; $MgCl_2$ 0.9; NaH_2PO_4 0.7; Glucose 5.6; Na pyruvate
711 2; HEPES 10, pH 7.4, 305 mOsm. This extracellular solution was complemented with 0.25
712 µM of apamin (Latoxan; cat # L8407) and 1 µM of XE-991 (Tocris Bioscience; cat # 2000) to
713 block SK channels and KCNQ4 channels, respectively. The external Ca^{2+} concentration was
714 increased from 1.3 to 5 mM to enhance the amplitude of Ca^{2+} currents to levels nearby body
715 temperature. All experiments were performed at room temperature (22°C–24°C).

716 Patch pipettes were pulled with a micropipette Puller P-97 Flaming/Brown (Sutter Instrument,
717 Novato, CA, USA) and fire-polished with a Micro forge MF-830, (Narishige, Japan) to obtain
718 a resistance range from 3 to 5 MΩ. Patch pipettes were filled with a cesium-based
719 intracellular solution containing (in mM): CsCl 145; $MgCl_2$ 1; HEPES 5; EGTA 1; TEA 20,

720 ATP 2, GTP 0.3, pH 7.2, 300 mOsm. Measurements of the resting membrane capacitance
721 (cell size) of IHCs were obtained in whole-cell voltage-clamp configuration at -70 mV and
722 after 2 min equilibrium of the internal patch-pipette recording solution with the IHC cytosol.
723

724 **BK currents**

725 Whole-cell recordings of BK currents were recorded in P30 and P365 IHCs from ex-vivo
726 whole-mount preparation (Skinner et al., 2003) as described above for Ca^{2+} currents.
727 Recording pipettes were filled with a KCl-based intracellular solution containing in mM: 158
728 KCl, 2 $MgCl_2$, 1.1 EGTA, 5 HEPES, and 3.05 KOH, pH 7.20.
729

730 **Intracellular Ca^{2+} imaging**

731 Fluorescent Ca^{2+} signals were measured with a C2 confocal system and NIS-element imaging
732 software (Nikon) coupled to the FN1 upright microscope as previously described (Vincent et
733 al., 2014 ; 2017). For Ca^{2+} imaging in IHCs, in which membrane capacitance and Ca^{2+}
734 currents were simultaneously recorded, patch pipettes were filled with the same cesium-base
735 solution described above supplemented with 50 µM of the red fluorescent indicator Rhod2
736 (R14220, Invitrogen™, Thermofisher Scientific). The Ca^{2+} dye was excited with a 543 nm
737 Helium Neon Laser system (Melles Griot 05-LGR-193-381) coupled to a Nikon C2-confocal
738 FN1- upright microscope and emission fluorescence at 552-617 nm was recorded at 18
739 images/s (resolution 0.4 µm/pixel). Using the Nikon imaging system NIS-Elements, IHC
740 active zones were first individually identified by their fluorescent transient responses,
741 following a 100 ms stimulation (from -80 to -10 mV) and then the focal plane (with pinhole
742 1.1 µm) was adjusted in the z dimension to give the brightest value for each active zone.
743 Then, after a 1 min rest, each active zone was stimulated by a train of five consecutive 100 ms
744 stimulation, each separated by 250 ms. Fluorescence emission in each active zone was
745 subsequently measured with ImageJ software by drawing a region of interest of 1 μm^2 at the
746 synaptic zone (Fig.9B). Emission fluorescent signals were analyzed and normalized by the
747 ratio $\Delta F/F_0$ ratio, where F_0 was the fluorescence level before stimulation.
748

749 **Statistical analysis**

750 Results were analyzed with OriginPro 9.1software (OriginLab, Northampton, USA). Results
751 were analyzed with OriginPro 9.1software (OriginLab, Northampton, USA). Data were tested
752 for normal distribution using the Shapiro-Wilk normality test, and parametric or

753 nonparametric tests were applied accordingly. For statistical analyses with two data sets, two-
754 tailed unpaired t-tests or two-sided Mann-Whitney tests were used. For comparisons of more
755 than two data sets, one-way ANOVA or two-way ANOVA followed by Tukey multiple
756 comparison test were used when data was normally distributed. If a data set was not normally
757 distributed Kruskal-Wallis tests followed by Dunn multiple comparison tests, respectively,
758 was used. When more than two data sets were compared and significant differences were
759 found, reported p values correspond to the post-hoc multiple comparison test. Values of $p <$
760 0.05 were considered significant. Results are expressed as mean ± SEM.
761

762 **REFERENCES**

763

764 **Bartolomé MV**, del CE, López LM, Carricondo F, Poch-Broto J, Gil-Loyzaga P. 2002.
765 Effects of aging on C57BL/6J mice: an electrophysiological and morphological study.
766 *Advances in oto-rhino-laryngology* **59**:106-11. doi: 10.1159/000059247

767 **Becker L**, Schnee ME, Niwa M, Sun W, Maxeiner S, Talaei S, Kachar B, Rutherford MA,
768 Ricci AJ. 2018. The presynaptic ribbon maintains vesicle populations at the hair cell afferent
769 fiber synapse. *eLife* **7**:e30241. doi: 10.7554/eLife.30241.

770 **Beurg M**, Michalski N, Safieddine S, Bouleau Y, Schneggenburger R, Chapman ER, Petit C,
771 Dulon D. 2010. Control of exocytosis by synaptotagmins and otoferlin in auditory hair cells.
772 *The Journal of neuroscience* **30**(40):13281-90.
773

774 **Brandt A**, Striessnig J, Moser T. 2003. $Ca_V1.3$ channels are essential for development and
775 presynaptic activity of cochlear inner hair cells. *The Journal of neuroscience* **23**(34): 10832-
776 10840.
777

778 **Campbell LW**, Hao SY, Thibault O, Blalock EM, and. Landfield PW. 1996. Aging Changes
779 in Voltage-Gated Calcium Currents in Hippocampal CA1 Neurons. *The Journal of*
780 *neuroscience* **16**(19):6286–6295.
781

782 **Defourny J**, Aghaie A, Perfettini I, Avan P, Delmaghani S, Petit C. 2019. Pejvakin-mediated
783 pexophagy protects auditory hair cells against noise-induced damage. *PNAS* **116**(16):8010-
784 8017.
785

786 **Delmaghani S**, Defourny J, Aghaie A, Beurg M, Dulon D, Thelen N, Perfettini I, Zelles T,
787 Aller M, Meyer A, Emptoz A, Giraudet F, Leibovici M, Dartevelle S, Soubigou G, Thiry M,
788 Vizi ES, Safieddine S, Hardelin JP, Avan P, Petit C. 2015. Hypervulnerability to Sound
789 Exposure through Impaired Adaptive Proliferation of Peroxisomes. *Cell* **163**(4):894-906. doi:
790 10.1016/j.cell.2015.10.023
791

792 **Del Nido PJ**, Glynn P, Buenaventura P, Salama G, Koretsky AP. 1998. Fluorescence
793 measurement of calcium transients in perfused rabbit heart using rhod 2. *The American*
794 *journal of physiology* **274**(2):H728-41.

Fernandez KA, Jeffers PW, Lall K, Liberman MC, Kujawa SG**.** 2015. Aging after noise exposure: acceleration of cochlear synaptopathy in "recovered" ears. *The Journal of neuroscience* **35**(19):7509-20. doi: 10.1523/JNEUROSCI.5138-14.2015.

Fingar DC, Salama S, Tsou C, Harlow E, Blenis J. 2002. Mammalian cell size is controlled by mTOR and its downstream targets S6K1 and 4EBP1/eIF4E. *Genes & development* **16**(12):1472-87.

Frank T, Khimich D, Neef A, Moser T. 2009. Mechanisms contributing to synaptic Ca2+ signals and their heterogeneity in hair cells. *PNAS* **106**(11):4483-8.

Fritzsch B, Duncan JS, Kersigo J, Gray B, Elliott KL. 2016. Neuroanatomical Tracing Techniques in the Ear: History, State of the Art, and Future Developments. *Methods in molecular biology* **1427**:243-62. doi: 10.1007/978-1-4939-3615-1_14.

Fu X, Sun X, Zhang L, Jin Y, Chai R, Yang L, Zhang A, Liu X, Bai X, Li J, Wang H, Gao J. 2018. Tuberous sclerosis complex-mediated mTORC1 overactivation promotes age-related hearing loss. *Journal of Clinical Investigation* **128**(11):4938-4955.

Fumarola C, La Monica S, Alfieri RR, Borra E, Guidotti GG. 2005. Cell size reduction induced by inhibition of the mTOR/S6K-signaling pathway protects Jurkat cells from apoptosis. *Cell death and differentiation* **12**(10):1344-57.

Grant L and Fuchs P. 2008. Calcium- and calmodulin-dependent inactivation of calcium channels in inner hair cells of the rat cochlea. *Journal of neurophysiology* **99**(5):2183-93. doi: 10.1152/jn.01174.2007.

Graydon CW, Cho S, Li GL, Kachar B, von Gersdorff H. 2011. Sharp Ca^{2+} nanodomains beneath the ribbon promote highly synchronous multivesicular release at hair cell synapses. *The Journal of neuroscience* **31**(46):16637-50.

Hafidi A, Beurg M, Dulon D. 2005. Localization and developmental expression of BK channels in mammalian cochlear hair cells. *Neuroscience* **130**(2):475-84

Hasson T, Heintzelman MB, Santos-Sacchi J, Corey DP, and Mooseker MS. 1995. Expression in cochlea and retina of myosin VIIa, the gene product defective in Usher syndrome type 1B. *PNAS* **92** (21) 9815-9819

Hequembourg S and Liberman MC. 2001. Spiral ligament pathology: a major aspect of age-related cochlear degeneration in C57BL/6 mice. *JARO* **2**(2):118-29.

Henry KR. 2002. Sex- and age-related elevation of cochlear nerve envelope response (CNER) and auditory brainstem response (ABR) thresholds in C57BL/6 mice. *Hearing research* **170**(1-2):107-15.

Hermann A, Sitdikova GF, Weiger TM. 2015. Oxidative Stress and Maxi Calcium-Activated Potassium (BK) Channels. *Biomolecules* **5**(3):1870-911.

Hu N, Rutherford MA, Green SH. 2020. Protection of cochlear synapses from noise-induced excitotoxic trauma by blockade of Ca2+-permeable AMPA receptors. *PNAS* **117**(7):3828-3838.

Hickman TT, Hashimoto K, Liberman LD, Liberman MC. 2020. Synaptic migration and reorganization after noise exposure suggests regeneration in a mature mammalian cochlea. *Scientific reports* **10**(1):19945.

Ison JR and Allen PD. 2003. Low-frequency tone pips elicit exaggerated startle reflexes in C57BL/6J mice with hearing loss. *JARO* **4**(4):495-504.

Ison JR, Allen PD, O'Neill WE. 2007 Age-related hearing loss in C57BL/6J mice has both frequency-specific and non-frequency-specific components that produce a hyperacusis-like exaggeration of the acoustic startle reflex. *JARO* **8**(4):539-50.

Jean P, Lopez de la Morena D, Michanski S, Jaime Tobón LM, Chakrabarti R, Picher MM, Neef J, Jung S, Gültas M, Maxeiner S, Neef A, Wichmann C, Strenzke N, Grabner C, Moser T. 2018. The synaptic ribbon is critical for sound encoding at high rates and with temporal precision. *eLife* **7**:e29275.

Jeng J, Johnson SL, Carlton AJ, De Tomasi L, Goodyear RJ, De Faveri F, Furness DN, Wells S, Brown SDM, Holley MC, Richardson GP, Mustapha M, Bowl MR, Marcotti W. 2020. Age-related changes in the biophysical and morphological characteristics of mouse cochlear outer hair cells. *The Journal of physiology* **598**(18):3891-3910.

Jeng J, Carlton AJ, Johnson SL, Brown SDM, Holley MC, Bowl MR, Marcotti W. 2021. Biophysical and morphological changes in inner hair cells and their efferent innervation in the ageing mouse cochlea. *The Journal of physiology* **599**(1):269-287.

Jiang XW, Li XR, Zhang YP. 2015. Changes of ribbon synapses number of cochlear hair cells in C57BL/6Jmice with age. *International journal of clinical and experimental medicine* **8**(10):19058-64. eCollection 2015.

Jing Z, Rutherford MA, Takago H, Frank T, Fejtova A, Khimich D, Moser T, Strenzke N. 2013. Disruption of the presynaptic cytomatrix protein bassoon degrades ribbon anchorage, multiquantal release, and sound encoding at the hair cell afferent synapse. *The Journal of neuroscience* **33**(10):4456-67. doi: 10.1523/JNEUROSCI.3491-12.2013

Johnson KR, Erway LC, Cook SA, Willott JF, Zheng QY. 1997. A major gene affecting age-related hearing loss in C57BL/6J mice. *Hearing research* **114**(1-2):83-92

Johnson SL, Marcotti W, Kros CJ. 2005. Increase in efficiency and reduction in Ca2+ dependence of exocytosis during development of mouse inner hair cells. *The Journal of Physiology* **563**(Pt 1):177-91.

Kazmierczak P, Sakaguchi H, Tokita J, Wilson-Kubalek EM, Milligan RA, Müller U, Kachar B. 2007. Cadherin 23 and protocadherin 15 interact to form tip-link filaments in sensory hair cells. *Nature* **449**(7158):87-91.

Kim KX, Payne S, Yang-Hood A, Li SZ, Davis B, Carlquist J, V-Ghaffari B, Gantz JA, Kallogjeri D, Fitzpatrick JAJ, Ohlemiller KK, Hirose K, Rutherford MA. 2019. Vesicular Glutamatergic Transmission in Noise-induced Loss and Repair of Cochlear Ribbon Synapses. *The Journal of neuroscience* **39** (23) 4434-4447; doi: 10.1523/JNEUROSCI.2228-18.2019.

Knipper M, Van Dijk P, Nunes I, Rüttiger L, Zimmermann U. 2013. Advances in the neurobiology of hearing disorders: recent developments regarding the basis of tinnitus and hyperacusis. *Progress in neurobiology* **111**:17-33. doi: 10.1016/j.pneurobio.2013.08.002.

Kros CJ, Ruppersberg JP, Rüsch A. 1998. Expression of a potassium current in inner hair cells during development of hearing in mice. *Nature* **394**(6690):281-4

Kujawa SG and Liberman MC. 2015. Synaptopathy in the noise-exposed and aging cochlea: Primary neural degeneration in acquired sensorineural hearing loss. *Hearing research* **330**(Pt B):191-9.

Kujawa SG and Liberman MC. 2019. Translating animal models to human therapeutics in noise-induced and age-related hearing loss. *Hearing research* **77**:44-52.

Kurt S, Sausbier M, Rüttiger L, Brandt N, Moeller CK, Kindler J, Sausbier U, Zimmermann U, van Straaten H, Neuhuber W, Engel J, Knipper M, Ruth P, Schulze H. 2012. Critical role for cochlear hair cell BK channels for coding the temporal structure and dynamic range of auditory information for central auditory processing. *FASEB journa*l **26**(9):3834-43.

Lagziel A, Ahmed ZM, Schultz JM, Morell RJ, Belyantseva IA, Friedman TB. 2005. Spatiotemporal pattern and isoforms of cadherin 23 in wild type and waltzer mice during inner ear hair cell development. *Developmental Biology* **280**(2):295-306.

Lang I, Jung M, Niemeyer BA, Ruth P, Engel J. 2019. Expression of the LRRC52 γ subunit (γ2) may provide Ca 2+-independent activation of BK currents in mouse inner hair cells. *FASEB journal* **33**(11):11721-11734.

Liberman LD, Wang H, Liberman MC. 2011. Opposing gradients of ribbon size and AMPA receptor expression underlie sensitivity differences among cochlear-nerve/hair-cell synapses. *The Journal of neuroscience* **19**;31(3):801-8.

Liberman MC and Kujawa SG. 2017. Cochlear synaptopathy in acquired sensorineural hearing loss: Manifestations and mechanisms. *Hearing research* **349**:138-147.

Liberman MC. 1982. Single-neuron labeling in the cat auditory nerve. *Science* **216**(4551):1239-41.

Lingle CJ, Martinez-Espinosa PL, Yang-Hood A, Boero LE, Payne S, Persic D, V-Ghaffari B, Xiao M, Zhou Y, Xia X, Pyott SJ, Rutherford MA. 2019. LRRC52 regulates BK channel function and localization in mouse cochlear inner hair cells. *PNAS* **116**(37):18397-18403.

Magupalli VG, Schwarz K, Alpadi K, Natarajan S, Seigel GM, Schmitz F. 2008. Multiple RIBEYE-RIBEYE interactions create a dynamic scaffold for the formation of synaptic ribbons. *The Journal of neuroscience* **28**:7954– 7967.

Matsubara A, Laake JH, Davanger S, Usami S, Ottersen OP. 1996. Organization of AMPA receptor subunits at a glutamate synapse: a quantitative immunogold analysis of hair cell synapses in the rat organ of Corti. *The Journal of neuroscience* **16**(14):4457-67.

Meyer AC, Frank T, Khimich D, Hoch G, Riedel D, Chapochnikov NM, Yarin YM, Harke B, Hell SW, Egner A, Moser T. 2009. Tuning of synapse number, structure and function in the cochlea. *Nature Neuroscience* **12**(4):444-53. doi: 10.1038/nn.2293. Epub 2009 Mar 8.

Michalski N, Goutman JD, Auclair SM, Boutet de Monvel J, Tertrais M, Emptoz A, Parrin A, Nouaille S, Guillon M, Sachse M, Ciric D, Bahloul A, Hardelin JP, Sutton RB, Avan P, Krishnakumar SS, Rothman JE, Dulon D, Safieddine S, Petit C. 2017. Otoferlin acts as a Ca^{2+} sensor for vesicle fusion and vesicle pool replenishment at auditory hair cell ribbon synapses. *eLife* **7**;6. pii: e31013.

Michel V, Goodyear RJ, Weil D, Marcotti W, Perfettini I, Wolfrum U, Kros CJ, Richardson GP, Petit C. 2005. Cadherin 23 is a component of the transient lateral links in the developing hair bundles of cochlear sensory cells. *Developmental Biology* **280**(2):281-94

Neef J, Urban NT, Ohn TL, Frank T, Jean P, Hell SW, Willig KI, Moser T. 2018. Quantitative optical nanophysiology of Ca_{2+} signaling at inner hair cell active zones. *Nature Communication* **9**(1):290. doi: 10.1038/s41467-017-02612-y.

Noben-Trauth K, Zheng QY, Johnson KR. 2003. Association of cadherin 23 with polygenic inheritance and genetic modification of sensorineural hearing loss. *Nature Genetics* **35**(1):21-3. Epub 2003 Aug 10.

Oliver D, Taberner AM, Thurm H, Sausbier M, Arntz C, Ruth P, Fakler B, Liberman MC. 2006. The role of BKCa channels in electrical signal encoding in the mammalian auditory periphery. *The Journal of neuroscience* **26**(23):6181-9.

Ouagazzal AM, Reiss D, Romand R. 2006. Effects of age-related hearing loss on startle reflex and prepulse inhibition in mice on pure and mixed C57BL and 129 genetic background. *Behavior Brain Research*. **172**(2):307-15. doi: 10.1016/j.bbr.2006.05.018.

Özçete ÖD, Moser T. 2021. A sensory cell diversifies its output by varying Ca 2+ influx-release coupling among active zones. *EMBO Journal* **1**;40(5):e106010.

Pujol R and Puel JL. 1999. Excitotoxicity, synaptic repair, and functional recovery in the mammalian cochlea: a review of recent findings. *Annals of the New York Academy of Sciences* **884**:249-54.

Pyott SJ, Glowatzki E, Trimmer JS, Aldrich RW. 2004. Extrasynaptic localization of inactivating calcium-activated potassium channels in mouse inner hair cells. *The Journal of neuroscience* **24**(43):9469-74.

Rousset F, Nacher-Soler G, Coelho M, Ilmjarv S, Kokje VBC, Marteyn A, Cambet Y, Perny M, Roccio M, Jaquet V, Senn P, Krause KH. 2020. Redox activation of excitatory pathways in auditory neurons as mechanism of age-related hearing loss. Redox Biology **30**:101434.

Roux I, Safieddine S, Nouvian R, Grati M, Simmler MC, Bahloul A, Perfettini I, Le Gall M, Rostaing P, Hamard G, Triller A, Avan P, Moser T, Petit C. 2006. Otoferlin, defective in a human deafness form, is essential for exocytosis at the auditory ribbon synapse. *Cell* **127**(2):277-89.

Sahoo N, Hoshi T, Heinemann SH. 2014. Oxidative modulation of voltage-gated potassium channels. *Antioxid Redox Signal* **21**(6):933-52. doi: 10.1089/ars.2013.5614. Epub 2013 Oct 26. Review

Sheets L, He XJ, Olt J, Schreck M, Petralia RS, Wang YX, Zhang Q, Beirl A, Nicolson T, Marcotti W, Trapani JG, Kindt KS. 2017. Enlargement of Ribbons in Zebrafish Hair Cells Increases Calcium Currents But Disrupts Afferent Spontaneous Activity and Timing of Stimulus Onset. *The Journal of neuroscience* **37**(26):6299-6313. doi: 10.1523/JNEUROSCI.2878-16.2017.

Siemens J, Lillo C, Dumont RA, Reynolds A, Williams DS, Gillespie PG, Müller U. 2004. Cadherin 23 is a component of the tip link in hair-cell stereocilia. *Nature* **428**(6986):950-5. Epub 2004 Mar 31.

Skinner LJ, Enée V, Beurg M, Jung HH, Ryan AF, Hafidi A, Aran JM, Dulon D. 2003. Contribution of BK Ca2+-activated K+ channels to auditory neurotransmission in the Guinea pig cochlea. *Journal of Neurophysiology* **90**(1):320-32.

Söllner C, Rauch GJ, Siemens J, Geisler R, Schuster SC, Müller U, Nicolson T; Tübingen 2000 Screen Consortium. 2004. Mutations in cadherin 23 affect tip links in zebrafish sensory hair cells. *Nature* **428**(6986):955-9.

Spassova MA, Soboloff J, He L, Hewavitharana T, Xu W, Venkatachalam K, van Rossum DB, Patterson RL, Gill DL. 2004. Calcium entry mediated by SOCs and TRP channels: variations and enigma. Review *Biochimica et biophysica acta* **1742**(1-3):9-20.

Spongr VP, Flood DG, Frisina RD, Salvi RJ. 1997. Quantitative measures of hair cell loss in CBA and C57BL/6 mice throughout their life spans. *The Journal of the Acoustical Society of America* **101**(6):3546-53.

Stamataki S, Francis HW, Lehar M, May BJ, Ryugo DK. 2006. Synaptic alterations at inner hair cells precede spiral ganglion cell loss in aging C57BL/6J mice. *Hearing research* **221**(1-2):104-18. Epub 2006 Sep 26

Taberner AM and Liberman MC. 2005. Response properties of single auditory nerve fibers in the mouse. *Journal of neurophysiology* **93**(1):557-69.

Thibault O and. Landfield PW. 1996. Increase in Single L-Type Calcium Channels in Hippocampal Neurons During Aging. *Science* **272** : 1017-1020.

Vincent PF, Bouleau Y, Safieddine S, Petit C, Dulon D. 2014. Exocytotic machineries of vestibular type I and cochlear ribbon synapses display similar intrinsic otoferlin-dependent Ca^{2+} sensitivity but a different coupling to Ca^{2+} channels. *The Journal of neuroscience* **34**(33):10853-69.

1004 **Vincent PF**, Bouleau Y, Petit C, Dulon D. 2015. A synaptic F-actin network controls
1005 otoferlin-dependent exocytosis in auditory inner hair cells. *eLife* **4**.

1006 **Vincent PF**, Bouleau Y, Charpentier G, Emptoz A, Safieddine S, Petit C, Dulon D. 2017.
1007 Different $Ca_V1.3$ Channel Isoforms Control Distinct Components of the Synaptic Vesicle
1008 Cycle in Auditory Inner Hair Cells. *The Journal of neuroscience* **37**(11):2960-2975.

1009 **Walton JP**, Frisina RD, Meierhans LR. 1995. Sensorineural hearing loss alters recovery from
1010 short-term adaptation in the C57BL/6 mouse. *Hearing research* **88**(1-2):19-26.

1011 **Wan G and Corfas G**. 2015. No longer falling on deaf ears: mechanisms of degeneration and
1012 regeneration of cochlear ribbon synapses. *Hearing research* **329**:1-10.
1013
1014 **Wang Y**, Tao J, Wang M, Yang L, Ning F, Xin H, Xu X, Cai H, Zhang W, Yu K, Zhang X.
1015 2019. Mechanism of Regulation of Big-Conductance Ca^{2+}-Activated K^+ Channels by mTOR
1016 Complex 2 in Podocytes. *Frontiers in physiology* **10**:167. doi: 10.3389/fphys.2019.00167.
1017 eCollection 2019.
1018
1019 **Willott JF.** 1996. Anatomic and physiologic aging: a behavioral neuroscience perspective.
1020 *Journal of the American Academy of Audiology* **7**(3):141-51.
1021
1022 **Wong HC**, Zhang Q, Beirl AJ, Petralia RS, Wang YX, Kindt K. 2019. Synaptic mitochondria
1023 regulate hair-cell synapse size and function. *eLife* **8**. pii: e48914. doi: 10.7554/eLife.48914.
1024
1025 **Zachary SP and Fuchs PA.** 2015. Re-Emergent Inhibition of Cochlear Inner Hair Cells in a
1026 Mouse Model of Hearing Loss. *The Journal of neuroscience* **35**(26):9701-6.
1027
1028 **Zheng QY**, Johnson KR, and Erway LC. 1999. Assessment of hearing in 80 inbred strains of
1029 mice by ABR threshold analyses. *Hearing research* **130**(1-2): 94–107.
1030
1031 **Zhou X**, Jen PH-S, Seburn KL, Frankel WN, and Zheng QY. 2006. Auditory brainstem
1032 responses in 10 inbred strains of mice. *Brain Research* **1091,** 16–26.

1033
1034
1035
1036
1037